

# Radiation Damage and the Design of Beam Intercepting Devices at CERN

Case Study: Interactions of 2 GeV Protons with Tungsten

by

RMM Welschen

to obtain the degree of Master of Science  
at the Delft University of Technology,  
to be defended publicly on March 25th, 2019.

Student number: 4161300  
Project duration: September 1, 2017 – August 31, 2018  
Thesis committee: Prof. dr. ir. J. Sietsma, TU Delft, supervisor  
Dr. ir. S.E. Offerman, TU Delft  
MSc. V. Marques Pereira, TU Delft  
ID. F Nuiry, CERN

*This thesis is confidential and cannot be made public until March 25th 2019.*

An electronic version of this thesis is available at <http://repository.tudelft.nl/>



# Preface

This thesis is the product of twelve months of research and engineering at CERN in Geneva. The framework of accelerator design is very particular but the work can be useful for anyone with an interest in estimating radiation damage effects in materials. I became interested in this topic at Técnico Lisboa during an introductory course of plasma science and technology where radiation damage can be a major problem. Coincidentally, the opportunity to design a proton beam intercepting device at CERN presented itself so I jumped at the chance to get involved. The aim of the work, described in this thesis, is to support particle physics experiments in dealing with this materials science challenge. The added value of this research is the result of applying a number of tools and investigation techniques that are playing an important role in current developments of the field of materials science and engineering. I learnt a great deal on presenting information from the people with whom I worked in science outreach and I am excited to apply it in this work on the design of beam intercepting devices for a CERN accelerator and radiation damage theory.

*RMM Welschen  
Geneva, August 2018*





# Abstract

In the framework of the High Luminosity LHC project at CERN, the need for further incorporation of evaluation of radiation damage into the design of beam intercepting devices at CERN is described and the risks of radiation damage in high energy applications are summarized. Radiation damage can be an important topic in high energy applications where doses to materials can accumulate up to the point where they start impacting device functionality and lifetime. The context of radiation damage at CERN provides unique circumstances that are not easily investigated experimentally. Simulation is an excellent alternative to study the behavior of particle transport in matter. For the LHC injector upgrade, proton beam energy levels, entering the Proton Synchrotron, are increased from 1.4 to 2 GeV. Using FLUKA Monte Carlo Simulations, the new energy deposition from the protons traversing a 2 cm thick tungsten plate is calculated. The proton beam is not entirely stopped, but the beam is sufficiently diluted to be outside of machine acceptance. Meaning, it can no longer be accelerated further. The energy deposition in the tungsten creates thermal stress waves. To evaluate the suitability of an alternative material, a thermo mechanical design of the plate is made in ANSYS with two different materials. Tungsten and the tungsten heavy alloy Inermet 180 (W-3.5%wt Ni-1.5%wt Cu) interactions with three different proton beams are evaluated. These beams are foreseen for Proton Synchrotron operation during high luminosity LHC. For single beam impact and normal operation mode the maximum temperature is 84 °C. For steady state, accidental impact, temperatures of 430 °C are reached. The maximum stresses are 145 MPa in Inermet 180 and 135 MPa in tungsten. Due to its brittle nature, it is advised to refrain from using tungsten within this stress range. To evaluate the radiation damage, the DPA and gas production are calculated, using the FLUKA Monte Carlo simulations. The peak DPA is 0.0035 and the peak gas production is 3.5 appm for hydrogen and 2.5 appm for helium. The average DPA production shows a clear maximum of DPAs just after the centre of the plate (1.18 cm depth from the surface). The maximum average hydrogen occurs after 1.2 cm and the maximum helium occurs more to the surface (0.2 cm depth). The peak concentrations are not entirely at the same location though this is where there would be higher risk of agglomerate formation just after the cascade. Since the peaks don't overlap the most critical radiation damage is likely to occur in an intermediate point.



# Acknowledgements

Discussions on high energy physics, the importance of fundamental research and working in a multidisciplinary team with colleagues from all over the world characterized the past year of my life and certainly I would not have reached this point without the support of many individuals. Firstly I would like to thank my supervisor Francois-Xavier Nuiry. He showed a large amount of patience and goodwill that finally allowed me to find the trajectory for my work. I am glad that he trusted me with the challenge of designing a device for the CERN accelerator complex and shared his experience in engineering for high energy physics experiments. Secondly my supervisor from TU Delft, Jilt Sietsma, granted me a large amount of freedom and trust. I am grateful for his questions, especially the ones to which I did not exactly know the answer so that I am driven to learn more. And then Viviam Marques Pereira spent a substantial amount of time with me to discuss the parts of my work that required challenge or further explanation. The fourth member, Erik Offerman also deserves a special mention because of his flexibility and patience in the entire process of graduation and besides that for transmitting his passion for teaching. Since I am not a physicist, some knowledge gaps relevant to my work needed bridging. I found a great amount of support from a couple of colleagues in the FLUKA section. Riccardo, Jose and Cesc during and outside of work hours explained concepts of high energy physics and mathematical descriptions of nuclear processes. Their effort is very much appreciated. Besides work, my time at CERN would not have been the same without the vibrance of the EN-STI-TCD section. Every single colleague has been helpful and friendly and many of them have given me an occasional Italian lesson. My office mates, Henry, Jaakko and Giulia in particular have helped me settle in so I felt at home and could begin the project directly. Besides my section, I was also adopted in the Neu6 consortium. Temporary but it has made a mark on the experience, Melanie, Tobias and Maris, I enjoyed staying with you a lot. I felt like I found the exact amount of curiosity, thoughtfulness and criticism I need on a daily basis. Special mention for Kuba, Branko, Vitesh, Stefan, Vignesh, Matias and Jaakko for taking the time to read and criticize my thesis. I would also like to thank the friends who took the time to come and visit me in Geneva. It was great to have a little dose of home and it also made me very happy to share this exciting time with you. Finally, being a summation of experience I need to thank my mother for never letting her love and care depend on my personal achievements and in that way creating an excellent feeding ground for developing individual interests. Her strong resilient character has taught me much about letting your decisions be lead by your norms and values. Secondly my brothers and sisters for being such interesting individuals and for teaching me the importance of including others. Following your passion, having lived and worked all over the world, without question, appreciating differences in culture and knowledge was a good lesson and helped me follow my passion and overcome practical hurdles. Looking back at the past year, it was a great time.



# Contents

Abstract	v
Acknowledgements	vii
1 Introduction	1
1.1 The Importance of CERN	2
1.2 The Framework: Particle Accelerator Design	3
1.2.1 Beam Intercepting Devices	3
1.3 Need for Research	4
1.4 Thesis Goals and Reader Trajectory	5
2 Literature Study	7
2.1 Fundamentals of Radiation Damage	8
2.1.1 Computing Radiation Damage Using Monte Carlo Simulations	9
2.1.2 Deriving an Energy Deposition Distribution Using Monte Carlo Simulations	10
2.2 Radiation Damage Effects in Tungsten	11
2.3 Case Studies and Scope Definition	12
2.3.1 Case 1: Beam-Material Interactions in Accelerator Components at CERN	12
2.3.2 Case 2: Energy Production Demonstrator Target Design	15
2.3.3 Case 3: China Spallation Neutron Source	16
2.3.4 Case 4: European Spallation Source	16
2.3.5 Experimental Evaluation of Changing Mechanical Properties	17
2.4 Overview	18
3 Thermo-Mechanical Studies	21
3.1 Simulation Conditions	21
3.1.1 Material Model	21
3.1.2 Beam Parameters	22
3.1.3 Energy Deposition	23
3.2 Thermo-Mechanical Simulations in ANSYS	24
3.2.1 FLUKA Energy Deposition Data Application in ANSYS APDL	25
3.2.2 Boundary Conditions	25
3.2.3 Mesh	26
3.2.4 Simulation Reliability	27
3.3 ANSYS Results	28
3.3.1 Thermal Simulations	28
3.3.2 Steady State	29
3.3.3 Structural	29
3.4 Discussion	31
4 Radiation Damage Simulation and Results	33
4.1 Preliminary Study	34
4.1.1 Microstructure Evolution With Cascades	34
4.1.2 FLUKA Monte Carlo Simulations	35
4.1.3 Computing the DPA Production in FLUKA	35
4.2 DPA and Gas Calculations	36
4.2.1 Tungsten	36
4.2.2 Tungsten and Inermet 180	40
4.3 Effects on Material Properties	41

---

5	Conclusion and Recommendations	43
5.1	Answering the Research Question. . . . .	43
5.1.1	Radiation Damage Problems in BID's . . . . .	43
5.1.2	Case Studies in Literature . . . . .	44
5.1.3	Investigation Techniques: The State of the Art . . . . .	44
5.1.4	Evaluating Radiation Damage Effects on BID Performance and Lifetime at CERN . . . . .	44
5.2	Recommendations . . . . .	45
	Bibliography	47
	List of Figures	51
	List of Tables	53
	Appendices	55

# Introduction

Studying radiation damage is important to numerous applications in different fields. Irradiation causes structural damage that can significantly modify material properties. Since energy deposition and radiation damage effects can cause failure of systems that are both costly and complex to recover the demand for materials that can resist radiation damage is increasing, in particular for nuclear energy, medical and aerospace applications. The effects of irradiation are an advantage in the treatment of cancer. Proton radiation allows for accurate reduction of tumors with reduced damage of surrounding tissue. By achieving more accurate simulation of hadron therapy, the treatment efficiency of cancer with proton irradiation can be improved.

Figure 1.1 shows an unwanted effect of radiation damage: blisters in steel that were obtained after hydrogen plasma irradiation. The radiation damage resulted in gas production and build up of gas concentrations close to the material surface lead to the formation of blisters. The demand for materials that can resist irradiation is increasing, in particular for nuclear, medical and aerospace applications. For example, high levels of radiation damage are limiting the lifetime of the DEMO fusion reactor blanket and divertor design requiring further research into enhancing materials capability to withstanding these high levels. The analysis of the materials' nuclear design requirements and the effects of radiation damage for candidate design options for DEMO are discussed by Federici et al. [1]. Their work also highlights the need for finding sufficient margins and improving material properties in order to enhance material irradiation resistance as well as enable accurate prediction of failure mechanisms and lifetimes.

When a spacecraft enters the upper layers of an atmosphere, the hypersonic velocity leads to the formation of plasma, causing radiation damage especially in materials present outside the spacecraft. Radiation in space is also an important factor that can induce failure. The damaging effects of cosmic rays to human tissue and their capacity to penetrate materials are demonstrated by Orlando et al. [3]. The risks associated with this constant irradiation are life-threatening and program-limiting. This creates a strong demand for creating a better understanding and quantifying the damage as well as further developing shielding material.



Figure 1.1: Optical micrographs of blisters on the surface of 95% deformed 13Cr2MoNbVB steel after irradiation with hydrogen plasma to  $2 \cdot 10^{24} \text{ H/m}^2$  at 275 (left), 305 (center) and 323 K (right). The micrographs are made for studying sputtering-induced erosion of plasma-facing materials (PFMs) for future commercial reactors. The scale is the same for all micrographs. [2]

This master thesis evaluates the radiation damage in a tungsten plate which is part of a safety mechanism inside the Proton Synchrotron (PS), one of the particle accelerators at CERN (figure 1.3). The methods are applicable to the design of other beam intercepting devices at CERN.

### 1.1. The Importance of CERN

Just as fundamental research is an important aspect of our society, feeding our curiosity and fruitfully advancing our everyday technologies such as GPS and medical imaging, fundamental research in turn is supported by advances in engineering. Physicists rely on the developments in state of the art technologies to experiment at high energy levels like the ones needed for high energy particle physics experiments.

The European Laboratory for Particle Physics, CERN (Le Conseil Européen pour la Recherche Nucléaire), is a European research laboratory that aims to answer the world's most fundamental questions such as, 'How do we explain the behavior of matter?', and to unite nations through science. The CERN convention was established just after World War II. It states a European nuclear physics research collaboration without military or commercial purposes and all its results are to be made public. As a driver of innovation, a provider of first-class education and a catalyst for peace, its societal impact is enormous. Florio et al. made an attempt at quantifying CERN's socio-economical impact and performed a cost benefit analysis for the LHC [4]. The total costs consisting of construction, machine upgrade and operation costs. The benefits are categorized into benefits to scientists, scientific knowledge as a public good, human capital from education and experience and finally benefits to the industry. Florio estimates that there is a 90% probability that benefits exceed costs with an expected value of 2.9 billion euro without considering the unpredictable applications of scientific discovery. In a report on the Impacts of Large Research Infrastructures on Economic Innovation and on Society the OECD mentions hadron cancer therapy research and development at CERN as one of the innovative technologies that demonstrates the organization's secondary contributions to society. [5] Figure 1.2 shows the simulation results of a proton therapy dose deposition using a Monte Carlo code that was originally developed for the physics experiments at CERN. Just like the world wide web, the capacitive touchscreen and the PET-scan, it was not part of the laboratory's principal scientific objectives. It is one of the many examples of technologies that were developed for physics and later came to benefit society in a different application.

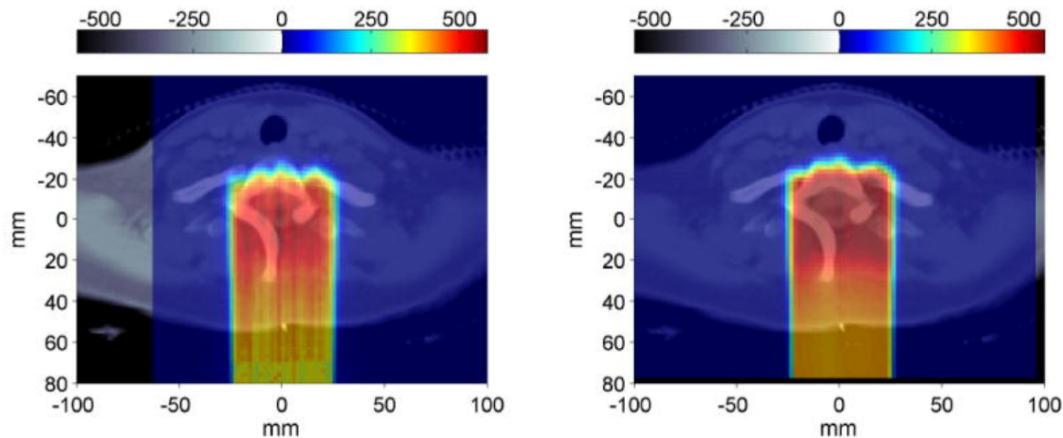


Figure 1.2: Monte Carlo calculated dose deposition (left) against the planned treatment (right). The top row shows a posterior-anterior field delivering 2 GyE to a tumor. The rainbow colour-bar displays dose values in mGy. The black-white colour-bar represents the HU map arbitrary rescaled for display purposes. [6]

Besides driving innovation, CERN facilitates excellent education and valuable work experience to employees and visiting researchers. Another important teaching activity is the science outreach to the general public and collaborations with educational institutes to research and develop science teaching around the globe. All year round teachers and students are invited to come to Geneva to participate in workshops and attend lectures at CERN. In this manner generations are brought together not only to share knowledge and best practices but also to discuss failures and challenging subjects like diversity and ethics in science. The high concentration of expertise and curiosity these activities achieve, help gain and spread ideas, understanding and knowledge throughout society. And that beyond measure is also an investment in human capital.



## 1.2. The Framework: Particle Accelerator Design

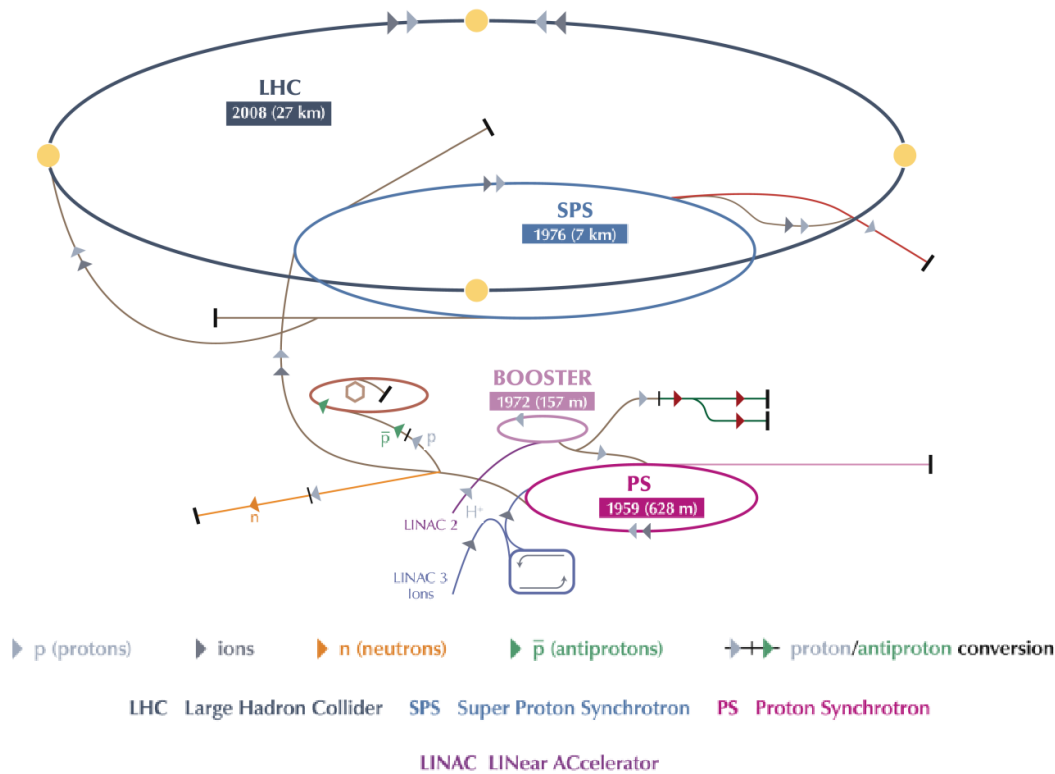


Figure 1.3: The CERN accelerator and experiment complex (modified from [7])

The most important machines at CERN are housed in the CERN accelerator complex, which is shown in figure 1.3. They enable experimental investigation of the theories of particle physics. For example in the LHC, protons collide at 13 TeV and data taken from these collisions helped prove the theory of Higgs et al. [8] that there is a particle (now named the Higgs boson) that is responsible for other particles having mass. Figure 1.3 shows the Linear Accelerator, LINAC 2, built at the beginning of this complex. This is the proton source where hydrogen gas is ionized, and the electrons are separated from the protons through a polarized field. Using their positive charge, the protons are further accelerated through a series of linear and circular accelerators which are designed to further accelerate and tune the flow of protons into beams with characteristics as requested by the experiments. Part of the CERN network of accelerators is the Proton Synchrotron (PS), a 59 year old machine that currently is designed to receive protons with energies up to 1.4 GeV from the Proton Synchrotron Booster (PSB). The PS can further accelerate these protons to energies up to 25 GeV into an experiment or into the Super Proton Synchrotron (SPS). The Super Proton Synchrotron (SPS) can further accelerate the proton beam to the TeV-range for higher energy experiments, and for injection into the Large Hadron Collider (LHC) or to targets of lower energy experiments.

### 1.2.1. Beam Intercepting Devices

Components inside the accelerators that are directly impacted by the beam or a part of the beam are called Beam Intercepting Devices (from now on referred to as BIDs). From interaction with high energy and high intensity beams, a BID in an accelerator may endure large amounts of radiation damage and energy deposition thus requiring careful design to be able to withstand these loads. The exact magnitudes of energy deposition and radiation damage the BID will incur are entirely dependent on its location within the accelerator complex, the type of material used and its utilization intensity. To illustrate the amount of energy a BID could intercept/receive: the accelerator fault tracker registered that in 2015 70 beams were dumped into BID's (beam dumps) in the LHC [9]. 70 beams containing 2808 bunches with an intensity of  $1.15 \times 10^{11}$  protons at 7 TeV each, results in 362 MJ per beam.

A beam stopper or beam dump is a BID that is designed to stop or diminish beams in a controlled manner. It acts as an accelerator protection and prevents high energy particles from causing undesired damage or activation downstream. Beams can either be steered into a dump or dumps can be placed into the beam trajectory. In order to achieve beams of certain shapes and intensities, the machines are highly tunable. And elaborate beam studies are done to find the settings that have the most desired effects on the beam. The Ralentsisseur is a dump that is dedicated to beam study operation mode inside the PS, where the beam characteristics are studied and tuned using sensors called secondary emission monitor grids (SEM-grids). These SEM-grids are extremely delicate and may only endure one interaction per bunch. To protect these SEM-grids from a second interaction, the beam needs to be dumped before it makes one entire turn inside the PS. This dumping is done by placing the Ralentsisseur (a beam stopper) into the beam trajectory.

The work presented here concerns the Ralentsisseur, a tungsten plate inside a vacuum chamber that is connected to the accelerator main vacuum pipe. The Ralentsisseur is located inside straight section 12 within the PS (figure 1.4a). Its functionality is to reduce the beam intensity level before it completes one turn inside the PS ring. Since the SEM-grids cannot endure more than a single high intensity interaction, the Ralentsisseur needs to be in place inside the vacuum chamber before the beam enters the PS. By placing the Ralentsisseur in the vacuum chamber, the proton beam is diluted and the SEM-grids are protected so they can continue to perform beam studies.

Figure 1.4a and 1.4b show the location of the Ralentsisseur and SEM-grids inside the PS and the current design of the Ralentsisseur in its vacuum chamber. The tungsten plate is moved into the beam aperture with a transverse movement. The active part that is in direct contact with the proton beam consists of a 20 mm thick Tungsten plate. It is designed as a beam stopper for protons with energies up to 1.4 GeV and it needs to be redesigned for protons with energies up to 2 GeV. This upgraded design should be completed before 2019 and shall be implemented in 2019 during the LHC Injectors Upgrade (LIU). [10, 11] The Ralentsisseur plate is attached to a pneumatic arm that moves it in and out of the beam trajectory with a SEM-grid interlock. The interlock ensures that the SEM-grids cannot be placed into the beam line unless the Ralentsisseur is in place to protect the SEM-grids from a second interaction after the beam is injected from the PSB into the PS.

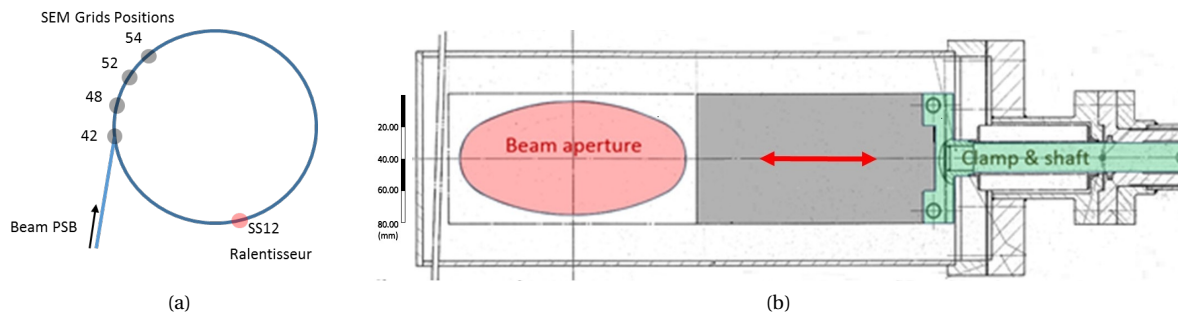


Figure 1.4: a: Proton Synchrotron ( $r=72\text{m}$ ) scheme showing the SEM-grid and Ralentsisseur positions. b: Working mechanism of the Ralentsisseur indicated with previous technical drawings [12].

### 1.3. Need for Research

As explained in the LIU Technical Design Report [13], the PS will be upgraded to meet the requirements of the High Luminosity LHC project. The injection energy from the PSB into the PS will be increased from 1.4 GeV to 2 GeV. This upgrade also requires the Ralentsisseur to be upgraded so that it can sufficiently dilute the beam and withstand the higher energy deposition along with the accompanying radiation damage.

At this moment there are no estimations for the foreseen radiation damage or structural damage from thermal stresses. But as the device is inside the PS beamline, a failure could cause an operational stop of the entire PS. Many CERN experiments rely on the PS beam, which cannot be supplied during an operational stop. Without a beam no data can be acquired by the researchers and this amounts to great losses to all those dependent on this data for their work. Experiments such as the LHC detectors (ATLAS, CMS, ALICE and LHCb), the High Radiation Materials facility, the anti-proton decelerator (see figure 1.3) are all dependent on the PS beamline and will incur great loss in case of an unforeseen operational stop.

To minimize the risk of failure of the Ralentsisseur, it is critical that the beam induced damage in the Ralen-

tisseur is conservatively estimated and that the device is designed with appropriate safety factors. A systematic evaluation of the effects of radiation damage for the design of BID's at CERN would benefit the device reliability. For example, for the design of the PS internal dumps the possible effects are mentioned. However, since there is a lack of relevant experimental data, the expected radiation damage is not further evaluated [12].

The effects of radiation damage can change material properties and thereby reduce the device's performance or in worse cases lead to failure. To prevent degradation and failure, the expected radiation damage effects on BID performance should be studied. For this work the following research question is formulated:

**How can radiation damage in materials be incorporated into the design of beam intercepting devices?**

This problem is divided into the following subquestions:

- What are the problems in BID's resulting from radiation damage?
- What relevant cases of radiation damage are described in literature?
- Which investigation techniques are currently used to evaluate radiation damage in these cases?
- Which tools can be used to evaluate radiation damage effects on BID performance and lifetime at CERN?

The research will be done within the framework of and parallel to the Ralentsisseur design. However, the research questions are posed more generally to emphasize the broader applicability of this work.

## 1.4. Thesis Goals and Reader Trajectory

Certain accelerator components will be exposed to high levels of radiation. Effects of the resultant radiation damage can include embrittlement, swelling, creep and hardening, which can negatively affect BID performance and worse, induce failure. To minimize the risk of failure of a BID at CERN this report focuses on estimating the radiation damage quantities and evaluating relevant effects on material properties. Subsequently they can be taken into account in the design, operation and maintenance of the BID. This is done in the framework of and in parallel to the Ralentsisseur design. By reviewing literature on radiation damage research in tungsten, the relevant issues in the Ralentsisseur are identified. Different investigation techniques are compared to establish a strategy to evaluate the effects of radiation damage on BID lifetime and performance. The Ralentsisseur thermo-mechanical design is done resulting in an understanding of the main design parameters and the operational temperatures and stresses in the tungsten plate. The goal is to extrapolated the limiting radiation damage values, regarding the effect of radiation damage on material properties, from simulation and experimental data. Chapter 2 gives radiation damage theory and the principles of calculating the energy deposition and radiation damage with a Monte Carlo code that simulates the transport of a particle through matter. Furthermore an overview of related case studies for proton irradiation at similar energy levels, using relevant materials and evaluating radiation damage is given. In chapter 3 the BID design method is given and the Ralentsisseur design is done. This method is based on the earlier work done by the section at CERN that is responsible for the design of BIDs. Finite Element Analysis software such as ANSYS is used, to simulate the BID in operation and calculate the resulting temperature changes and thermal stresses. The simulation conditions, such as material model, beam parameters and energy deposition are given. Finally the resulting data is discussed and evaluated. Chapter 4 explains the evolution of cascades and how they create defects in the material lattice. The behavior of these defects within the microstructure is explained and qualitative relations with changes in material properties are given. The DPA and gas production is computed using FLUKA, a Monte Carlo particle tracking code. The quantities are evaluated separately after which the gas/DPA ratio is discussed. To investigate an alternative material for the difficult to machine and brittle tungsten, DPA and gas production for both tungsten and Inermet 180 (W-3.5%wt Ni-1.5%wt Cu) are calculated. A comparison is made between the DPA and gas production values in the two materials. In chapter 5 a summary of the results is given, the research questions are answered and recommendations for future research and finetuning the BID design method are provided.



## Literature Study

The studies, with regards to fundamental physics, that can be done at CERN are directly related to the beam characteristics that are achieved inside the accelerators. For example, one important characteristic is the beam emittance. A measure for the beam dimensions (spatial particle spread), the emittance is a key parameter for the overall performance of an accelerator. The experiments that are done in the LHC require a large amount of data in order to perform the statistical analysis that can prove for example a particle discovery. The more collisions take place, the more data is generated. And as we achieve a higher density proton beam the chance of a collision is increased and so a smaller spatial particle spread means that there is a higher chance of proving the theories that can be an explanation for why our universe looks the way it does. Studying the emittance already starts in the LHC injectors such as the Proton Synchrotron (PS). And monitoring emittance allows for matching the beam to the PS-machine vacuum chamber and surrounding instruments. Furthermore, by studying the emittance, beam instabilities can be detected and fed back into the control systems to help achieve a higher luminosity and therefore allow for higher energy experiments to take place [14]. To study the emittance in the PSB to PS transfer line, SEM-grids are installed inside the transfer line and PS. The transverse beam emittance and matching may be obtained from beam profiles measured at four different SEM-grids provided the beam only crosses the SEM grids once [15]. The Ralentsisseur is a tungsten plate inside a vacuum chamber in the Proton Synchrotron that acts as a beam 'retarder' and will incur direct impact of the proton beam. During its lifetime it will be impacted by a total of  $9.2 \cdot 10^{18}$  protons. The protons traverse the Tungsten plate of the Ralentsisseur which reduces the beam energy levels such that it is outside of machine acceptance. This means that the particles are outside of the energyrange of particles that can be further accelerated inside the proton synchrotron.

To achieve better emittance, the accelerator components need to be upgraded. For the upgrade of the Ralentsisseur a new design is prepared and the radiation damage levels are estimated and taken into account. Further literature research is needed to understand the design of BIDs and to find the state of the art of technology that can be designed to withstand radiation damage. The objectives of this literature research are formulated as follows:

- To determine the BID design method.
- To gain an understanding of the impact of radiation damage on the device's performance, reliability and lifetime estimations.
- To investigate radiation damage research on other relevant radiation damage scenarios.
- To analyse benchmarked simulation data from similar radiation damage problems that can lead to qualitative assessments on changes of the material structure and properties.
- To implement this knowledge and achieve a method to evaluate the radiation damage during the design of Beam Intercepting Devices.

The results of this literature research are finally used to more precisely estimate the device lifetime and performance in later chapters. Currently, the method of designing the Ralentsisseur and other BIDs at CERN

is based on best practices of the EN-STI-TCD (targets, collimators and dumps design for the engineering department group working on sources, targets and interactions) section at CERN [16, 17].

In this chapter a comparison is made between this method and how comparable BID's have been designed in other organizations. Knowledge gained in other nuclear facilities, for example in neutron spallation sources and nuclear reactors can provide useful insight. Especially benchmarked simulations and experimental results from other nuclear facilities can provide valuable insight into radiation damage behavior since physical data is much less common for accelerator radiation damage studies. The focus for these cases, in this report, lies in how radiation damage is taken into account during the design process. Both investigation techniques, based on simulation as well as based on experiments, are discussed. Finally the discussion summarizes and compares different strategies to design BIDs and evaluate beam induced damage.

## 2.1. Fundamentals of Radiation Damage

When a high energy proton traverses a volume it interacts with the matter on its trajectory. Due to these interactions an energy deposition occurs, resulting in a local temperature increase and displacement of particles and atoms in the interacting material. A challenging aspect in estimating the energy deposition and radiation damage on a nuclear level is that for different energy levels interactions between particles change and other interaction mechanisms may become more important. Meaning that as the particle traverses and loses its energy, the interaction it has with the material changes. For example at higher energy levels a good approximation for nuclear stopping power in a crystalline target is Rutherford scattering (pure coulombic interaction). An excellent explanation of why this is the case is given by C. Race [18] and G. Was [19]. Because the primary particle has such high energies, its cross section is relatively small and it will therefore only barely interact with the surrounding nuclei, allowing it to travel some distance. During this time the particle loses energy, mostly through interaction with surrounding electrons. This is called channeling. The damage at this point may be caused by ejected electrons (coulombic explosion model), transfer of electron heat to surrounding ions (thermal spike model) or excitation of electrons weakening bonding forces where the surrounding material is strained and the resulting pressure causes damage. Eventually the channeling particle has lost sufficient energy and its cross section has become bigger. It now interacts with surrounding ions and defects on its path. As it interacts with another ion either another (sub)cascade is formed or cascade evolution begins. For lower energies, effects of electrons in the internuclear space become more relevant and pure coulombic scattering is no longer accurate enough. The energy loss of protons below 1 GeV takes place through inelastic processes with atoms while for protons with energies higher than 1 GeV most energy losses happen through nuclear interaction where stopping powers in between these interactions also remain an important contribution to the process [20]. The focus in this work is on the higher energy range proton-matter interactions in the range of hundreds of MeV to several GeV. In this work radiation damage is defined as the formation of a vacancy and self interstitial atom (SIA) pair (Frenkel pair) due to an energy deposition that is equal to the threshold energy (the minimum energy needed to move an atom from its place creating a Frenkel pair). This energy is dependent on the displacement direction and can be measured along principal axes or averaged over all directions. It is determined for many materials both experimentally and using simulation methods such as molecular dynamics [21]. The point defects can diffuse and affect the formation and evolution of 2D and 3D defects that can act as a sink for these point defects. They can recombine or be absorbed by sinks such as a void, dislocation, dislocation loop, grain boundary or precipitate. The recombination and reaction of a vacancy or interstitial into or with a defect sink is described by chemical rate equations:

$$\frac{dC_v}{dt} = K_0 - K_{iv}C_iC_v - K_{vs}C_vC_s \quad \frac{dC_i}{dt} = K_0 - K_{iv}C_iC_v - K_{is}C_iC_s \quad (2.1)$$

Where

$C_v$  = vacancy concentration

$C_i$  = interstitial concentration

$K_0$  = defect production rate

$K_{iv}$  = vacancy-interstitial recombination rate coefficient

$K_{vs}$  = vacancy-sink reaction rate coefficient

$K_{is}$  = interstitial-sink reaction rate coefficient

These equations are difficult to solve analytically because they are nonlinear differential equations and because of the difference in  $K_{is}$  and  $K_{vs}$ . This difference comes from the much more mobile nature an interstitial has with respect to that of a vacancy. [19] There are more interstitial sites to jump to than there are

vacancy sites and interstitial bonding is in general weaker than bonds between lattice points. When considering a pure metal, with Frenkel pairs being created, and where low T and low sink density is assumed. A build up of point defects occurs which after some time stabilizes due to recombination. As interstitials are more mobile they are absorbed by sinks at a higher speed which makes the interstitial concentration decrease while the vacancy concentration increases. During continuous irradiation, production, recombination and absorption of interstitials takes place in parallel and a steady state is reached. The same occurs for vacancies, however since the mobility of vacancies is much different, their recombination and absorption rates are slower and the vacancy concentration reaches higher steady state values than interstitials. For further information, the influence of temperature and sink density is well explained through schematics in Was et al. [19] Despite the transitions of the reactions actually occurring a lot slower, the schemes highlight the main ideas surrounding the point defect equilibrium and the effect of the different reaction rate coefficients on point defect concentrations. For example that increasing the sink density reduces the amount of time where interstitial and vacancy recombination dominates point defect concentrations because sinks will start to contribute to point defect annihilation much sooner. Another observation is that at high temperatures ( $T/T_m \geq 0.5$ ) the increased recombination rate at sinks keep the interstitial concentration low. And even though interstitial concentration is lower at steady state, the interstitial and the vacancy contribution to atom mobility is equalized because of the faster diffusion rate of interstitials.

Another issue during irradiation, is that transmutation can result in the formation of foreign atoms like Re, Os, Ta, He and H. The transmutation of element A into element B occurs through a nuclear reaction where the particles on both sides of the equation are balanced as seen in equation 2.2.

$${}_y^x A = B + \frac{4}{2} \alpha \quad (2.2)$$

Where  $B = \frac{x-4}{y-2} A'$ .

In recent literature, more and more scientists have expressed concerns regarding the effects of transmutation elements in irradiated materials. Zhao et al. [22] gives an overview of literature that studies the origin, behavior and effects of transmutation elements on material properties. Much work has been done on the effects of Re, Os and Ta on the crystal structure, mechanical properties and thermodynamics of tungsten. The effects of Re, Os and Ta (from now on referred to as TE, which stands for transmutation elements) on H/He behavior were investigated. The TE atoms' formation was simulated in both interstitial and substitutional sites (IS and SS). The formation energy in an IS is much higher meaning atoms prefer to stay at an SS and are also more stable there. Therefore all TE's can be assumed to be located at SS's. The study also shows that Re and Os increase the bulk modulus (the ratio between the change in pressure and the fractional volume compression) of W, while the bulk modulus decreases with Ta concentration. TE's showcase the tendency to lower the Young's modulus while enhancing the ductility and Poisson's ration of tungsten The formation energy of He shows that it prefers SS sites while H prefers the tetrahedral interstitial site. This variation occurs because of the difference in the element electron orbits. Due to these interactions, the diffusion path of He and H are changed. The further away the He and H are from other TE's, the easier they diffuse. [22]

### 2.1.1. Computing Radiation Damage Using Monte Carlo Simulations

The chance in a game of solitaire drove Stan Ulam to the idea to use the new Electronic Numerical Integrator and Computer to perform statistical sampling to solve neutron diffusion and multiplication problems in fission reactors. Figure 2.1 gives a schematic of trajectory decisions based on the probabilities of the different outcomes for the event in question. For example,  $g_L$  gives the distribution of paths that a particle can follow before interacting with another nucleus with the shorter distances being more probable than the longer distances. These values are dependent on material properties while  $g_k$  on the other hand gives probabilities for different types of interactions to occur. These are dependent on the particle energy. [23] Monte Carlo method changes the process described by an integral into a number of random operations. The behaviour of a large population is described with sampling and statistics. In this work, the Monte Carlo method is used to calculate particle trajectories and resulting radiation damage and transmutation.

The transport of a particle through matter is essentially described by the Boltzman transport equation (equation 2.3) where the probability of having a specific set of particles under certain circumstances is related to a specific collision taking place. The change of the location of particles  $f$  is described by an external forces term, a diffusion term and a collision term. Since the proton beam and nuclear interactions comprise such large populations, it would be computationally inefficient to compute the solution to the Boltzman equa-

tion for all particles involved. Utilizing the Monte Carlo method, trajectories for a sample of this population can be computed. Through statistical analysis, this sample leads to an approximation of the solution of the Boltzman equation for the total interaction of a population of protons within a body is achieved. Numerous Monte Carlo codes to track particle transport have been developed. The main codes being MCNPX, GEANT4, FLUKA, MARS, PHITS. The difference in the codes being in the implementation of the physics models [24]. A further in depth explanation of how FLUKA computes the radiation damage is given in chapter 4.

$$\frac{df}{dt} = \left(\frac{df}{dt}\right)_{force} + \left(\frac{df}{dt}\right)_{diffusion} + \left(\frac{df}{dt}\right)_{collision} \quad (2.3)$$

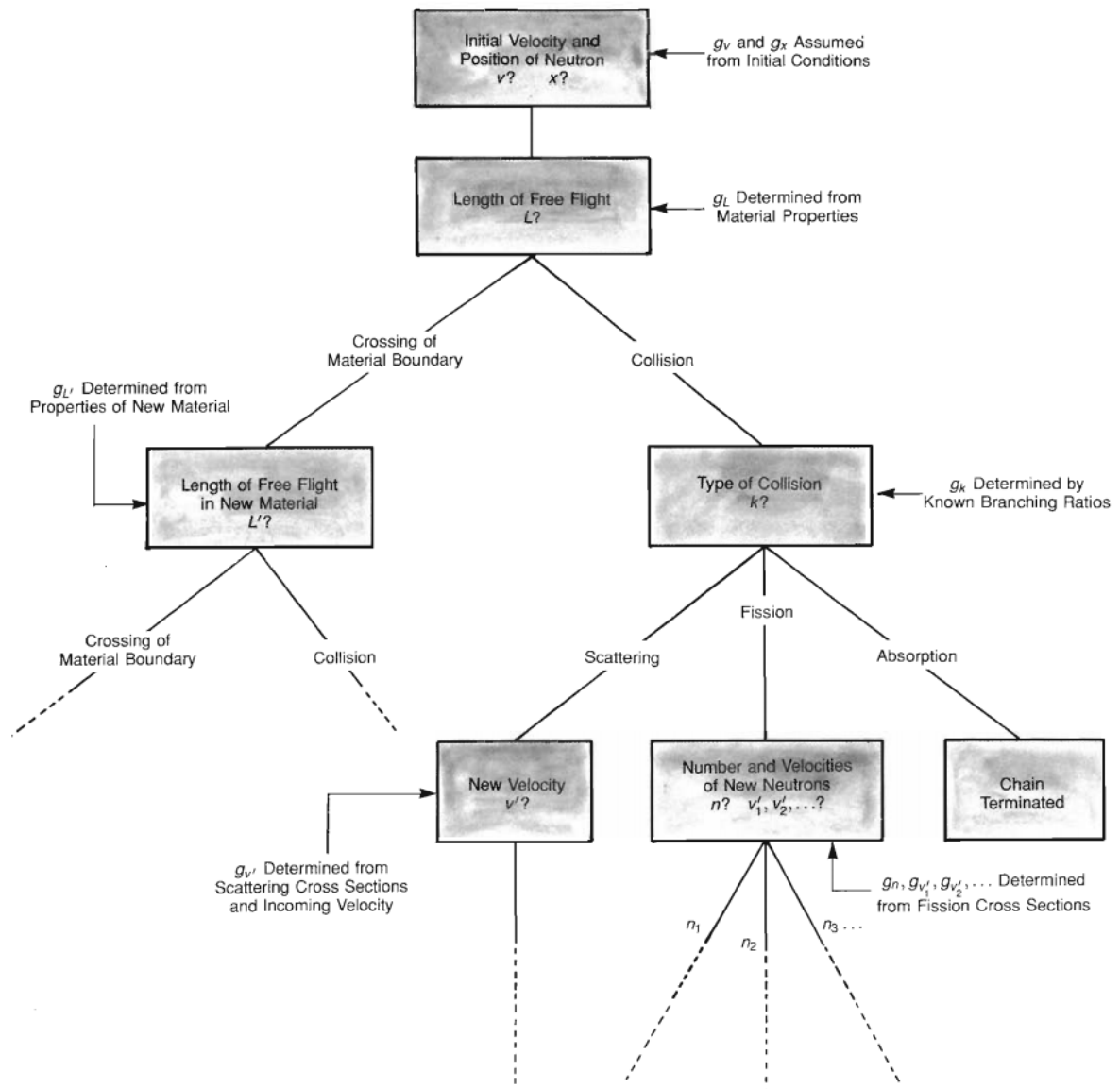


Figure 2.1: The history of each neutron is generated by making various decisions about the physical events that occurs as the neutron goes along. [23]

### 2.1.2. Deriving an Energy Deposition Distribution Using Monte Carlo Simulations

As a primary particle is traveling through a body, the interactions with the matter result in a thermal load. To simulate the thermal load of a beam intercepting device, the energy deposition distribution is needed. The proton beam hitting the tungsten plate is simulated using the FLUKA Monte Carlo code. Proton trajectories are computed by taking into account the most important interaction mechanisms within the material [12].



Subsequently, this energy distribution map is applied as a load to the volume elements of our finite element model in ANSYS. Thermal and structural finite element simulations are performed and give an estimation of the temperature and stress distributions over time. Importing the FLUKA results into ANSYS is further discussed in section 3.2.1. FLUKA tracks a number of mechanisms through which it interacts with the material and at the same time deposits energy. As the primary proton traverses the Ralentsiseur tungsten plate, it loses energy amongst others by creating cascades and particle showers on its way. When the shower components cannot travel further, the cascade energy is considered deposited. In the high energy density deposition region, close to the beam axis, produced electrons and ions are the main result of the deposited energy [25]. This ionization occurs through inelastic scattering, where an electron is emitted through coulombic interaction with the proton and through charge absorption where the proton is absorbed by an atom nucleus and an alpha or beta particle is emitted. Further away from the beam axis, heavy products and recoils of neutron-nuclear interactions are more important for the energy deposition (figure 2.2). Numerous studies go further in depth on the physics of the beam-material interactions [19, 26, 27, 20].

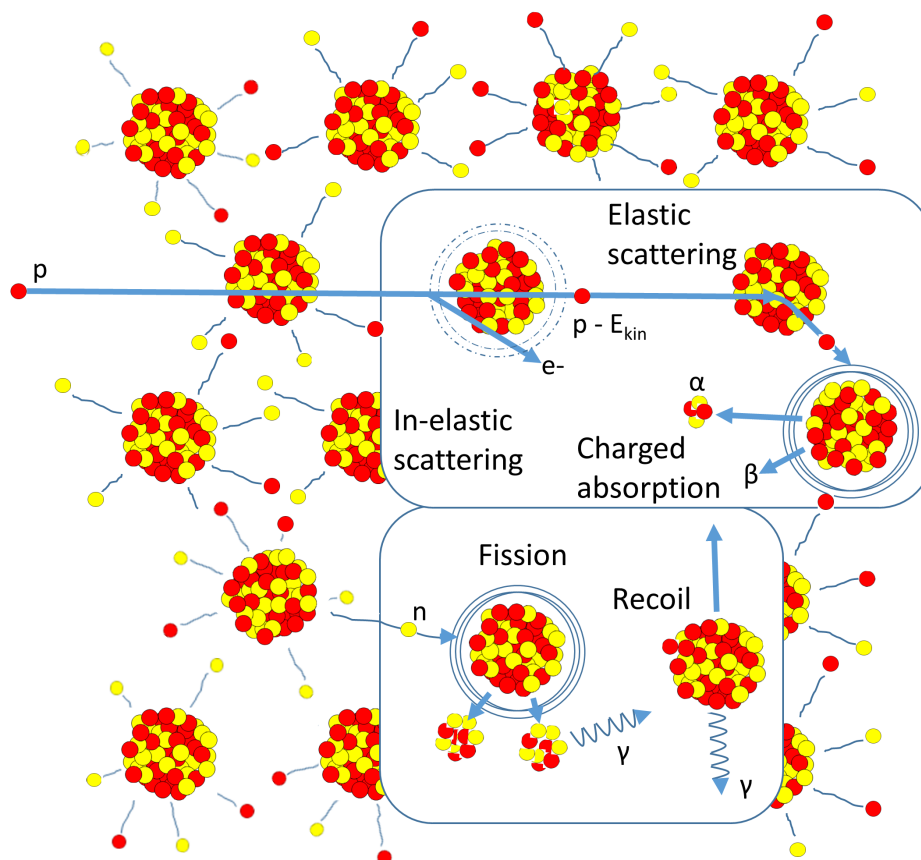


Figure 2.2: Overview of the most important energy deposition mechanisms for thermo-mechanical studies using FLUKA energy deposition maps as a thermal load.

## 2.2. Radiation Damage Effects in Tungsten

Critical radiation damage effects in tungsten include hardening, embrittlement, yield strength decrease, swelling, void and even blister formation. An example of such blisters can be seen in figure 2.3. Radiation damage in tungsten is much researched for different nuclear reactor applications at lower energy levels. However, different interaction mechanisms become important at different energy levels. For example the cross section of total and elastic p-p and p-n scattering show that at higher energy levels fewer elastic p-p collisions occur [26]. This complicates the application of knowledge and experimental data acquired from lower energy beam-material interactions and pushes towards a focus on the specific energy regime that the Ralentsiseur is exposed to.

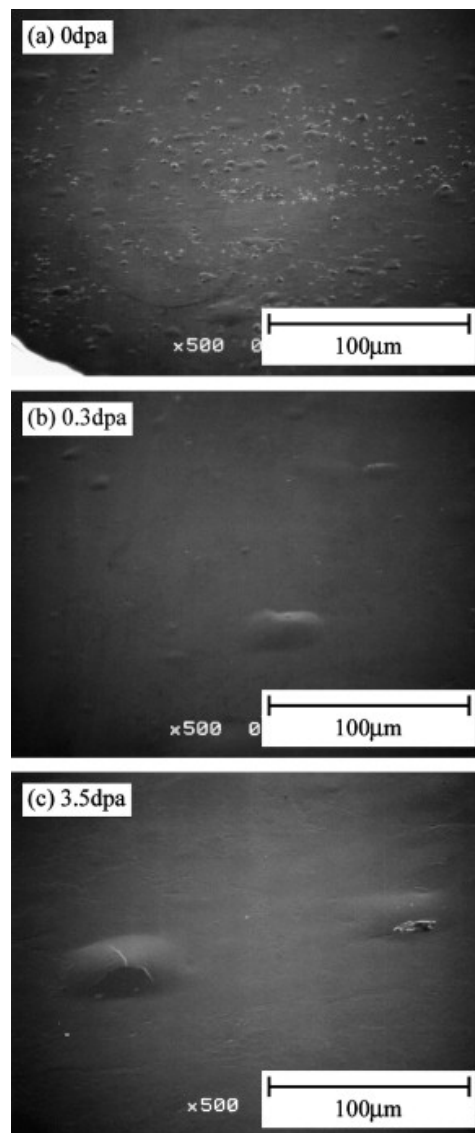


Figure 2.3: SEM photograph of the tungsten samples with (a) 0 DPA, (b) 0.3 DPA, and (c) 3.5 DPA damage after mixed H<sup>+</sup>, C<sup>+</sup> ion beam irradiation. [28]

## 2.3. Case Studies and Scope Definition

The design of a BID begins with the understanding of the beam-material interactions at subatomic and atomic scale. During the design process of a BID, the occurring mechanisms and how a change in the material structure due to radiation damage leads to a change in properties is taken into account.

In this section, state-of-the-art BID designs are discussed. The aim is to discuss the approaches followed that are relevant to the Ralentsisseur and the aspects that were taken into account during the design process. From these approaches the scope of this work is determined.

### 2.3.1. Case 1: Beam-Material Interactions in Accelerator Components at CERN

Future generation medium- and high-energy accelerators call for the research on high energy beam-material interactions. In their paper [26] Mokhov (Fermilab) and Cerutti (CERN) discuss how effects in materials under irradiation can influence the lifetime and performance of a BID. An indication of the beam impact risks is derived through thermo-mechanical studies. First, a worst case scenario beam impact is simulated using a Monte Carlo Transport simulation code. The code models interactions with matter while the particle is transported through a material. Each interaction results in an energy deposition. Depending on the amount of

energy deposition, particle showers are created causing further cascades resulting in more energy deposition until the cutoff energy is reached. At this point the particle is assumed to have insufficient energy for further transport and is stopped. Its remaining energy is deposited at its final position. The statistical chance that a particle undergoes a specific interaction results in particle trajectories for the amount of particles in the beam (for example in the order of  $10^{13}$  protons). This then results in transient energy deposition values throughout the material volume undergoing beam impact. In the next step this energy deposition is imported into a Finite Element Method software package. In transient thermo-mechanical models this energy deposition is applied to the nodes throughout the body and the resulting change in temperatures and thermal expansions in the body are calculated. Finally, the thermal stresses are evaluated. Material responses that are relevant to component lifetime and operational performance are thermal shock and quasi-instantaneous damage, insulation property deterioration due to dose build-up, radiation damage from atomic displacements as well as helium and hydrogen production, detector component radiation aging and damage, superconducting magnet quenching, single event effects in electronics, detector performance deterioration and radioactivation. For BID's where there is a strong indication that further radiation damage studies are needed, radiation damage is taken into account during the design phase. This is done by using the Monte Carlo simulations to calculate the production of displacements per atom (DPA). These DPAs are a measure for Frenkel pairs, an atom or ion leaving its place in the lattice and lodging nearby in the crystal (creating a vacancy and an interstitial), characteristic radiation damage defects. Helium and hydrogen can amplify the effects of radiation damage. The uncertainties for hydrogen production are around 20%, where the uncertainties for helium production is around 50%. Gas calculations were for example done for the SHiP Target. A block consisting of titanium-zirconium-molybdenum alloy (TZM) and tungsten plates with 5 mm gaps for cooling water to run through. The target is impacted by  $4 \times 10^{13}$  450 GeV protons. Figure 2.4 shows the beam sweep footprint. The beam trajectory (going into the page) is adjusted so that it hits the SHiP target in a spiraling manner rather than having the entire beam hit the target in one point. This is done to optimize the target functionality and lifetime.

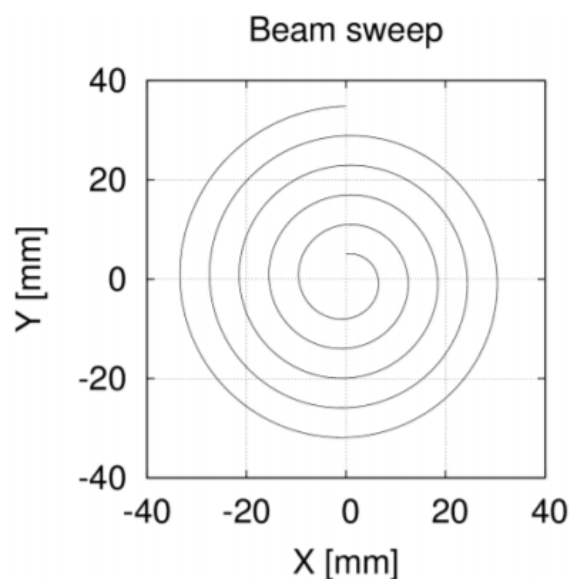


Figure 2.4: The figure shows the assumed beam sweep footprint at the longitudinal position corresponding to the SHiP target. [29]

In figure 2.5 the energy deposition is plotted. It shows a discontinuity, a sudden increase of energy deposition in the plate just after 60 cm. This is where the target plates are made of Tungsten. Tungsten having a higher density explains the increase in energy deposition. Because the beam has more interaction with the material, more energy is deposited.

The peak energy deposition per pulse is  $844 \text{ J/cm}^3/\text{pulse}$ . Because of the high amount of protons expected during the target lifetime ( $2 \times 10^{20}$ ), a significant amount of change of mechanical properties due to radiation damage is expected. Figure 2.6 shows the simulation results regarding DPAs achieved during the target lifetime. A maximum value of 0.9 DPA is reached in TZM. The maximum DPA achieved in tungsten is about 0.7. The gas production values are plotted in figure 2.7. The peak values of 430 appm hydrogen and

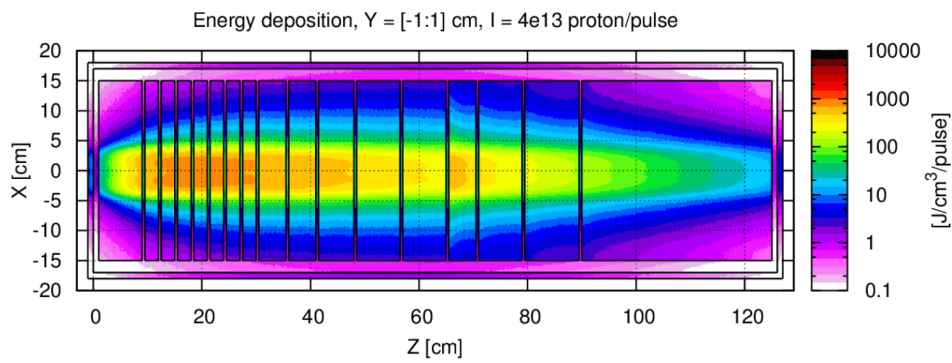


Figure 2.5: The figure shows the energy density along the Z direction but averaged along the horizontal direction 2 cm around the beam centre. [29]

150 appm helium are reached in TZM though a sudden increase is clearly visible in the transition to tungsten. The maximum gas/DPA ratios are 800 and 299 appm /DPA for hydrogen and helium in TZM and 690 and 305 appm/DPA for hydrogen and helium in tungsten. Particularly helium production can further reduce the lifetime of a component dramatically because of its low solubility in the crystal lattice, it forms clusters, accumulates defects and dislocations. Both gasses contribute to swelling and in some cases blister formation close to the surface.

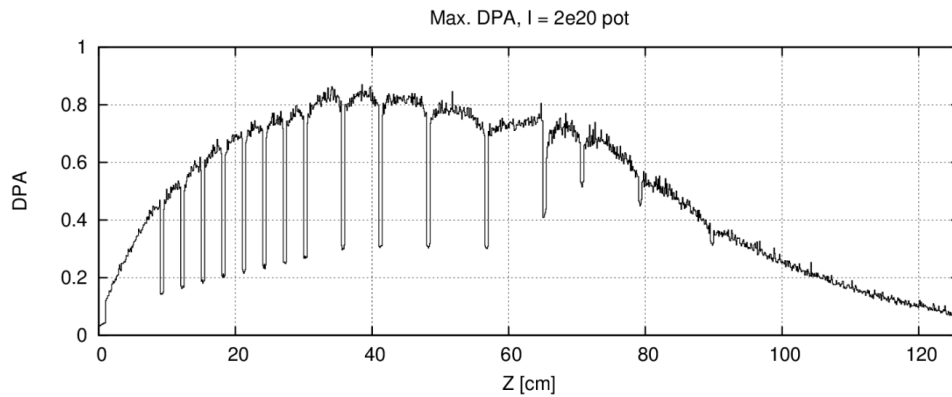


Figure 2.6: The figure shows the maximum DPA along the longitudinal (Z) direction. [29]

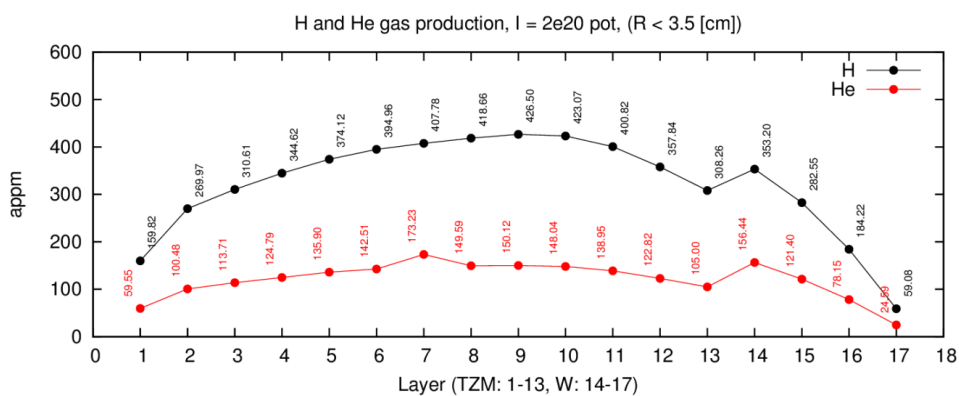


Figure 2.7: Overview of the most important energy deposition mechanisms for thermo-mechanical studies using FLUKA energy deposition maps as a thermal load. [29]

Mokhov and Cerutti [26] present the change of beam material interaction due to radiation damage as a lifetime influencer, but it is not mentioned in their list of factors in operational performance. However, the Fermilab antiproton production target and its drop in productivity with damage are extensively discussed.

For this target irradiation induced swelling in the titanium jacket of the target and in the region where the titanium jacket was visibly damaged with a 15% drop in the measured antiproton yield. The visible damage of the titanium jacket affected the functionality by decreasing the yield and it is reasonable to also assume that a swelling as a result of radiation damage may significantly affect the functionality. Deriving the decrease in functionality from simulated radiation damage values would allow for a better understanding of the different roles the various effects are playing when it comes to a reduced antiproton yield.

For the Antiproton Decelerator target design, radiation damage was evaluated in iridium [30]. The effects will lead to target failure due to a loss of density in the central part of the target rod. Radiation damage is also the main cause of decrease in anti-proton yield up to 20% observed after weeks of operation due to void formation, swelling and loss of density. Swelling peaks at intermediate temperatures (

$$0.3T_m < T < 0.5T_m <$$

) and lower temperatures cause low defect mobility limiting the growth of voids while at higher temperatures void growth is limited due to recombination of vacancies. A second inducer of void formation are stresses in the material. Also radiation embrittlement and radiation induced creep is discussed. The formation and accumulation of noble gases seem to be the dominating cause. Especially by intergranular fracture when the gas atoms migrate to grainboundaries. Embrittlement is observable from 1ppm and saturated above 10 ppm. In heavy metals such as iridium, rhenium and tungsten, bubble formation is accelerated by Kr and Xe formation from spallation due to a higher Z. Stresses inside the material are calculated coupling ANSYS with FLUKA where plasticity is neglected. More radiation studies are available for CERN detectors, sensors, electronics, polymers and composites presumably since these parts are more visibly affected and more often failing [31, 32, 33, 34, 35].

For the design of the PS dump core, J. Esala did material selection and thermo-mechanical studies for graphite and CuCrZr [12]. The exiting beam, energy deposition and radiation damage are studied using the FLUKA Monte Carlo code. Thermo mechanical simulations were done to compute the temperature and stress states with a 25 ns High Luminosity LHC beam. First a thermal simulation was done, after which it was verified by comparing energy deposition as applied in ANSYS to how it was calculated by FLUKA. The values that are used for comparison are total deposited power, total deposited energy and peak energy deposition. As temperatures and stresses were close to critical values, mesh sensitivity studies were performed for the graphite block. The performance of a cooling system was evaluated using a steady state simulation where the scenario of continuous beam impact is simulated. A peak temperature of 1381 °C is reached in graphite and 157 °C in CuCrZr. The effect of a geometry change to allow for material expansion shows higher temperatures, higher tensile stresses but lower compressive stresses. The possible radiation damage effects on the different materials are discussed, but qualitative values for changes in material properties under similar irradiation damage were not found for the materials in question. The radiation damage was not considered in the material model of the simulations. The gas production due to beam impact is not mentioned. The thermal expansion is caused by the temperature increase from the energy that is deposited by the proton interaction and resulting particle showers. This chapter explains the computation of the temperature increase and thermal stresses following these interactions with the help of Thermo-Mechanical finite element analysis (FEA) in ANSYS. Furthermore the FLUKA energy deposition maps and their application in ANSYS are given. More implications of the energy-deposition maps and FLUKA Monte Carlo simulations are discussed in chapter 4.

### 2.3.2. Case 2: Energy Production Demonstrator Target Design

The design of a heavy metal target is studied for the Energy Production Demonstrator (EPD) and Material Testing Station (MTS) optimization [36]. Tungsten, thorium and natural uranium interaction with proton beams having an intensity of  $6.25 \cdot 10^{15} p/s$  are studied for different energy levels. The aim for the MTS is to maximize the DPA (DPA is explained in section 2.3.1) and gas production. Figure 2.8b shows that the  $DPA/E_p$  (DPA-proton energy ratio for both materials) was highest for the 1-4 GeV energy range and figure 2.8a shows the  $He/DPA/E_p$  was the highest for  $U^{NAT}$  and Th at 1 GeV and below 1 GeV for W. A thermal ANSYS study using the MARS15 code to generate heat deposition maps showed there is a possibility that meltdown will occur in the target. This issue was solved by altering the target design. The new design was verified by new thermal ANSYS simulations.

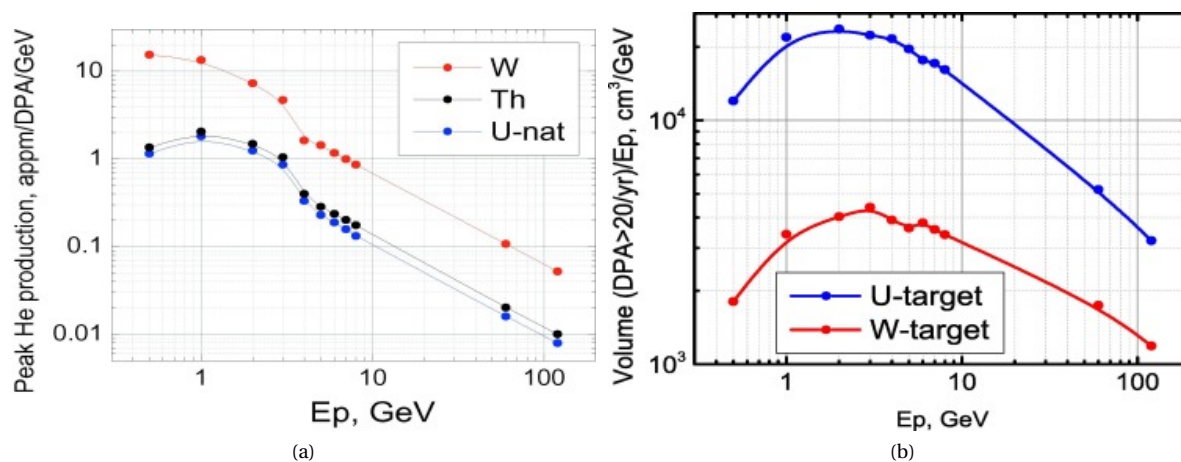


Figure 2.8: a: Helium ( ${}^2\text{He}_4$  and  ${}^2\text{He}_3$ ) production in the targets. b: Displacement per atom (DPA) volume in the targets.

### 2.3.3. Case 3: China Spallation Neutron Source

Recent studies on radiation damage in tantalum clad tungsten by a 1.6 GeV proton beam were done by Dong-Dong Pan et al. for the China Spallation Neutron Source (CSNS) [37]. The radiation damage and gas production were estimated with MCNPX2.5.0 and a comparison was made between two different beam profiles. Peak displacements and gas production is given in table 2.1. The high amounts of gas production results in swelling and embrittlement. Maximum DPA values were derived from experimental work performed by Maloy et al. [38], where the change of ductility with dose was measured for tungsten.

Beam shape	DPA/y	Target		
		He (appm/y)	H (appm/y)	He/DPA (appm/DPA)
Uniform	2.2	123	768	56
Gaussian	5.5	353	2141	64

Table 2.1: DPA and gas production values for a 1.6 GeV 100 kW gaussian and uniformly shaped proton beam operating 5000 hours per year.

The same authors responsible for the work above also published calculations of He and H concentrations from beam impact on the CSNS target [39]. This time, FLUKA Monte Carlo code was used to simulate the production rates. The calculated He cross section of W is compared to 0.75 GeV experimental data and the loading on microcracks due to increased H or He accumulation near crack tips is discussed.

### 2.3.4. Case 4: European Spallation Source

Mora et al. evaluated the activation and radiation effects for the European Spallation Source W target. A 2 GeV proton beam impacts a solid rotating target made of tungsten blocks. Tungsten was chosen partly due to experience accumulated over the years at kW range. Using the MCNPX Monte Carlo Code, the DPA in the tungsten target was acquired by considering incident protons as well as generated neutrons (see figure 2.9). The calculated DPAs are evaluated using existing experimental data.

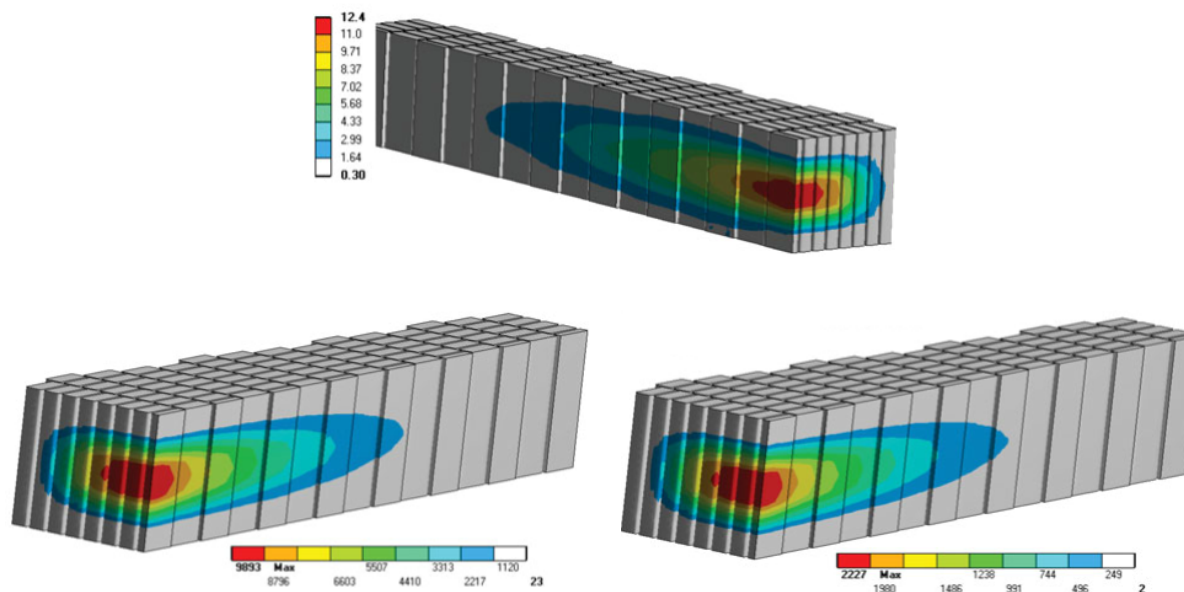


Figure 2.9: DPA (top), H (left) and He (right) production in the ESS target after 5 years of operation, Proton beam profiles along horizontal and vertical directions employed for the calculations. Such profiles correspond to those contained within the current machine specification. [40]

The H and He production throughout the target elements is calculated (figure 2.9) and a swelling of 0.22% is expected. The effects on material properties are extrapolated from existing data. The W target should be replaced when radiation damage values exceed 3-4 DPA which suggests a lifetime of 5 years. The impact of gas production is hard to assess due to lack of experimental data at these temperature ranges. Embrittlement and fracture surfaces where gasses may accumulate require further study.

### 2.3.5. Experimental Evaluation of Changing Mechanical Properties

Maloy et al. irradiated high purity tungsten rods with an 800 MeV, 1mA proton beam for six and two months. [38] Fluence was determined with activation foil analysis. After which simulation fluence was adjusted to match the isotope production. Calculated helium and hydrogen content as a function of dose are shown in figure 2.10a. The relations are more or less linear. Stress strain relations of the tested radiation dose ranges are made for the two different sample diameters and the results are shown in figure 2.11a and 2.11b. The yield strength increases quite dramatically with just several DPAs. The effect on the hardening coefficient seems less dramatic. Cracking of compression tested irradiated samples was found. Samples tested at 475 °C also showed an increased tendency for non-uniform deformation.

The results for 2.6 and 3.2 mm diameter samples differed somewhat because they came from different batches of material. A difference in material grade or even surface finishing can already be significant. However, work hardening after yielding is identical in both material grades. Furthermore, values below 5 DPA resulted in similar yield stresses (1600 MPa). For a higher DPA range, yield increases significantly and the drop following yield decreases. The variation in  $T_{irr}$  (50 - 270 °C) is minimal compared to  $T_{melt}$  and is therefore unlikely to be responsible for the change observed in the mechanical response. A general trend is for the yield strength to increase rapidly with doses up to a few DPA and then increase slowly with dose as is shown in figure 2.10b. The general dependence of yield strength of tungsten on dose is the same as that for RT tests but the magnitudes of the values are lower, probably due to changes in dislocation dynamics. For values above 20 DPA, the helium content was about 2000 appm. The effects of helium on tungsten properties is under discussion. There is work on the effects of helium on steel tensile properties which indicates that helium would have an effect on the compressive deformation behavior of tungsten as well.



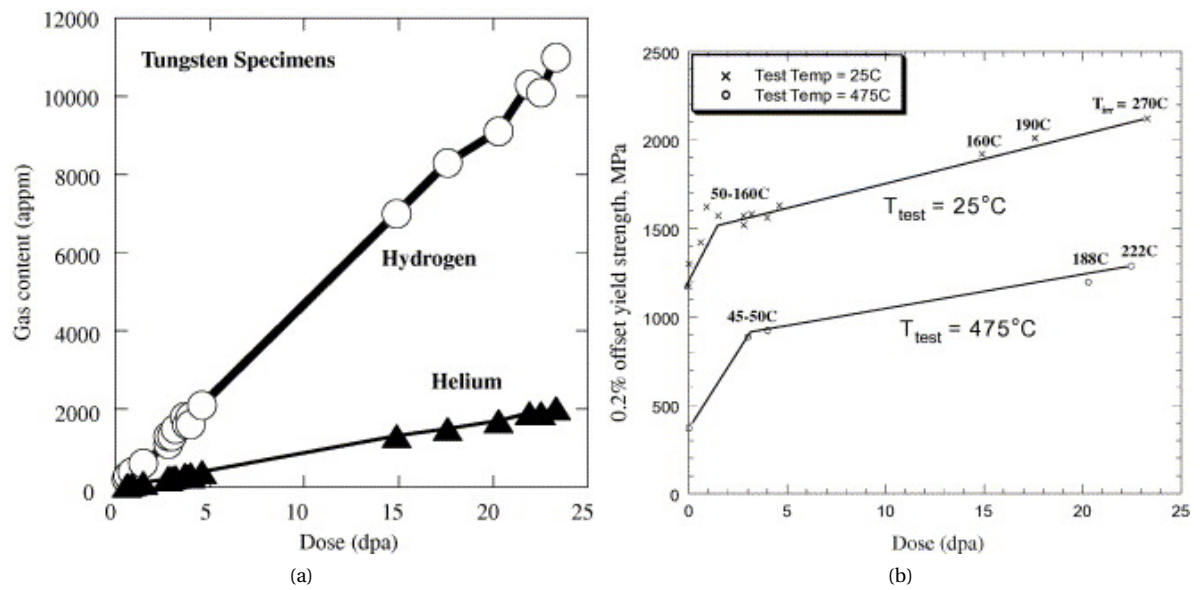


Figure 2.10: a: Calculated helium and hydrogen content of the samples plotted as a function of dose. b: Graph plotting 0.2% yield stress vs. dose for compression tests on tungsten irradiated up to 23 DPA at 50–270°C and a test temperature of 25°C.[38]

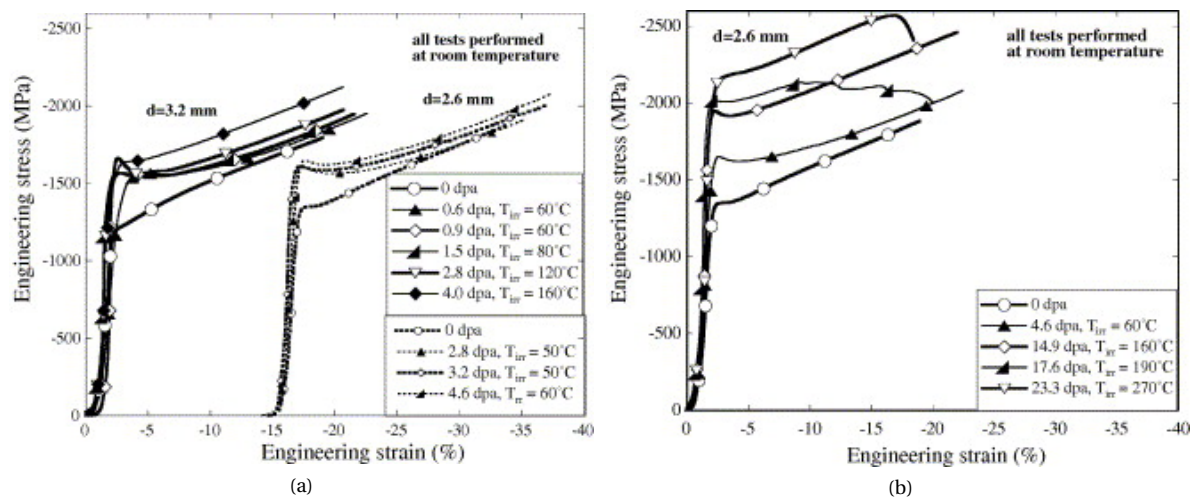


Figure 2.11: a: Graph showing engineering stress/strain curves for tungsten irradiated to 4.6 DPA and compression tested at room temperature. Tests are divided into specimens with 3.2 mm diameter and 2.6 mm diameter. The two different size specimens were made from different heats of tungsten. Data were gathered continuously. The plot markers are an aid to distinguishing between the different tests. b: Graph showing engineering stress/strain curves for tungsten tested in compression at room temperature after irradiation in a proton beam from doses ranging from 0 DPA to 23 DPA. Data were gathered continuously. The plot markers are an aid to distinguishing between the different tests.[38]

## 2.4. Overview

The radiation damage studies for the SHiP target (section 2.3.1) has evaluated the maximum DPA values in the longitudinal (Z) direction. To evaluate gas production, the average values for gas production over a target plate volume corresponding to the maximum radius of the diluted beam were computed. Subsequently the average gas per maximum DPA value was calculated. These calculations assume that the produced gas will diffuse and spread homogeneously throughout the central volume of the plate. However, diffusion of gas is very much dependent on temperatures achieved. In the case where no sufficient diffusion takes place, concentrated values of gas production can lead to higher gas/DPA production and more dramatic radiation damage effects. Further studies into how the produced gas is distributed are required to achieve conservative radiation damage estimations.



To study radiation damage, the energy production demonstrator at Fermilab aims to maximize the DPA radiation damage as well as the gas production [36]. An extremely high flux ( $6.25 \cdot 10^{15}$  p/s) resulted in maximum DPA values around 2 - 3 GeV and peak helium production below 1 GeV, indicating a maximum helium to DPA production ratio between 1 and 3 GeV.

The problem of radiation damage can be applicable to many scenarios. To confine this study, the scope is limited to BIDs at CERN. One particular BID, the Ralentisseur, is studied and in this framework the design method is investigated and utilized resulting in the Ralentisseur upgraded design. Thermo-mechanical design is performed along with coordination of the project regarding the design with parties involved, e.g. the vacuum group. Numerous studies for radiation damage in Tungsten exist, however since the radiation damage is highly dependent on the type of irradiation and the energy and temperature at which irradiation takes place, the focus lies with studies that were performed at a similar energy range (i.e. hundreds of MeV to several GeV). Unfortunately, the number of studies fitting these requirements is limited.

Monte Carlo simulations can be used to compute the DPA and gas production. The amount of DPA being produced is already often evaluated. The challenge seems to be studying radiation damage on a meso-scale. It is not exactly understood how damage on a nuclear level exactly relates to changes in the microstructure and how it affects material properties. Limited experimental work is done for higher energy level irradiation. Benchmarking of gas production simulations can improve the accuracy of the estimations for helium and hydrogen production (currently the accuracy is to 20% and 50% respectively). Models to study the effect of helium and hydrogen on micro-structure and material properties are needed.

Two cases were found for proton-tungsten irradiation at similar energy levels. The China Spallation Neutron Source and the European Spallation Source both performed studies to predict the lifetime of tungsten including radiation damage estimations. Monte Carlo simulations were performed to calculate DPA, H and He production. To achieve a lifetime estimation, experimental results relating DPA to stress-strain curves and yield strength increase were used. For the China Spallation Neutron Source the influence of gas production on micro-cracks is studied. The effect of gas production in the European Spallation Source target is still being evaluated.



## Thermo-Mechanical Studies

Radiation damage experiments can require complicated set-ups, time and a large budget, not easily available for every problem at CERN, simulations are an excellent alternative to study the behaviour of a material interacting with high energy particles. In general, if the engineering problem allows for it studying the Thermo-Mechanical stresses using FEA can be a relatively low cost, rapid way to gain insight thermal stress values.

FEA software such as ANSYS Workbench and Monte Carlo particle tracking code such as FLUKA, is a combination of mathematical models that can produce quick estimations of thermo-mechanical material behavior with proton beam impact. Requiring minimal resources (a regular desktop suffices) and offering a great amount of flexibility (the work is not that much bound to a time and place, current everyday technologies allow for the work to be done in the office or on the road), the effects of radiation damage in materials can be studied. Finally, by using existing benchmarking data it is possible to estimate the effects on material properties from simulated DPA and gas production results. This gives more accurate material models and allows the design of beam intercepting devices while also taking into account radiation damage. The current Ralentsisseur plate is made of tungsten. However, since pure tungsten is a relatively hard to machine, brittle material, the well machinable, ductile alloy, Inermet 180 (W-3.5%wt Ni-1.5%wt Cu, from now on referred to as IT180) is also investigated to determine whether it is a suitable alternative. In order to design the Ralentsisseur for its new energy levels the interactions of the beams with the geometry and a tungsten and IT180 material model are computed. During these interactions, a part of the proton energy is deposited into the material. This energy deposit results in a local temperature rise, causing expansion and thermal stresses travelling throughout the material. This chapter discusses the simulation of the change in temperature and resulting thermal expansion and stresswaves throughout the tungsten plate of the Ralentsisseur.

### 3.1. Simulation Conditions

The simulation conditions are set up with the help of the general requirements and working conditions[41, 10], previously defined in documents by CERN. Estimations for future beam characteristics inside the Proton Synchrotron (e.g. number of protons per pulse and pulse time) are given by the CERN Beams department [41]. A substantial amount of consulting was done with the CERN Beam department since it will in the end be responsible for the Ralentsisseur operation for beam studies.

#### 3.1.1. Material Model

Currently, the plate material is tungsten which has a high density. Meaning, the traversing proton beam will interact with a large number of atoms on its path. And so we will have a more efficient reduction of beam energy. With an increase in interactions on its path a proton is also more deflected from its original path. Furthermore, tungsten has a high thermal shock resistance, i.e. it can sustain a certain degree of thermal differential strains without yield or fracture occurring and the melting temperature is high, making it a robust solution for this specific application with high rates of very localized energy deposition and high temperature gradients. However, tungsten is a very brittle material making it difficult to machine and nowadays commercially available tungsten alloys like IT180 (Inermet180) are much easier to machine. The performance of IT180 to that of tungsten the beam interaction with both materials is modelled and a comparison is made.

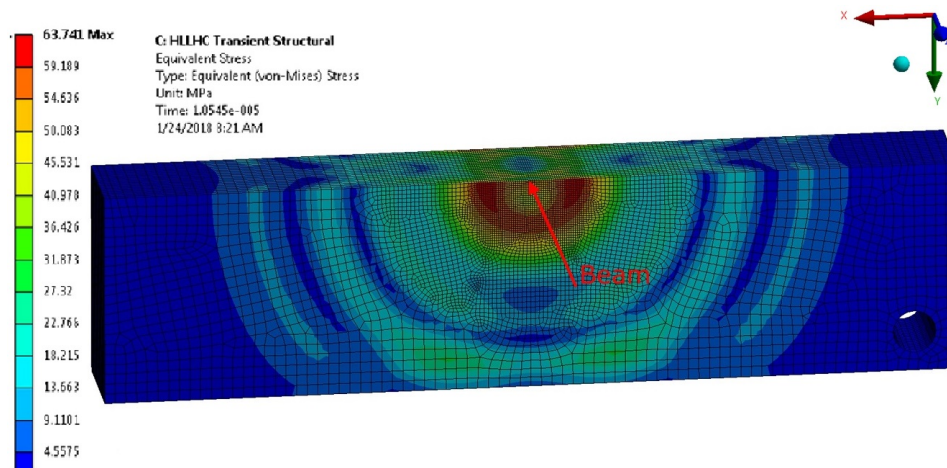


Figure 3.1: A stresswaves in the Ralentsisseur tungsten plate from intercepting a 2 GeV proton beam.

In ANSYS and FLUKA, the material models in table 2 are used. The IT180 material models from published data are not complete and therefore it is necessary to make some additional assumptions regarding the material properties. For example, due to lack of characterization data for IT180 Bertarelli et al. used pure tungsten material models to perform Monte Carlo and thermo-mechanical simulations to assess damage thresholds of IT180 components impacted by high intensity high energy beams depositing energies up to  $10^3$  GeV/cm<sup>3</sup> [42]. However the goal of the simulations for the Ralentsisseur design is to also evaluate the difference between tungsten and IT180 performance and so the real material properties shall be used. The density, Young's Modulus, Poisson's Ratio, Thermal Conductivity, Specific Heat and Yield Strength are available for room temperature and will be assumed constant with temperature. Only for emissivity no values are known and so the emissivity for tungsten is assumed. The tungsten properties varying with temperature originate from material databases (CES Selector 2015 and MPDB v7.71). The conditions under which the properties were obtained were chosen to fit the Ralentsisseur conditions as much as possible. The IT180 properties originate from the supplier. A more detailed overview of the material model and sources can be found in appendix A.1.

Property	Tungsten		IT180	
	20°C	800°C	20°C	600°C
Density (kgm <sup>-3</sup> )	19290	19090	18000	-
Young's Modulus (GPa)	400	364	360	-
Poisson's Ratio	0.28	0.29	0.28	-
Thermal Conductivity (Wm <sup>-2</sup> ·K <sup>-1</sup> )	164	120	110	-
Emisivity	0.02	0.13	0.02	0.13
Specific Heat (Jkg <sup>-1</sup> ·°C <sup>-1</sup> )	132	150	135	-
Mean Coefficient of Thermal Expansion (μ°C <sup>-1</sup> )	4.4	4.8	5.23	5.45
Yield Strength (MPa)	1320	76	615	-
Maximum Service Temperature (°C)			825	

Table 3.1: Summary of material properties of pure tungsten and IT180 (properties obtained from, Plansee SE, CES Selector 2015 and MPDB v7.71)[43]. More extensive list of material properties and sources can be found in appendix A.1.

### 3.1.2. Beam Parameters

The energy deposition load on the Ralentsisseur is determined by the impacting beam. In the Ralentsisseur Functional Specifications [10] (see also the beam specifications in appendix A.2), the beam intensity,  $I$ , (total number of protons per beam) is given. However, one important parameter, the beam spotsize, (horizontal,  $\sigma_x$  and vertical,  $\sigma_y$ ) is not defined. In 2017, the Beams department published beams [41] that are foreseen

to be injected into the PS during its operation after the LHC injectors upgrade. The beam characteristics for the most relevant beams are given in table 3.2. A beam can be more critical to a material depending on the spotsize, intensity and pulse time and therefore the beams with the most critical spotsizes and intensities are taken as an approximation for the worst case scenario impact to the Ralentsisseur. Four different beams are chosen. This also allows us to study the effect of spotsize and intensity variation on the tungsten plate performance. A worst case scenario for the energy deposition was used to compute the DPA and beam intensity after interaction with the plate. This worst case scenario is computed as the theoretical maximum pulse intensity with the smallest known spot size (BCMS spot size). The bunch period  $t_{bunch}$ , the timeframe during which a bunch hits the plate and the pulse time  $t_{pulse}$ , the time it takes for a new bunch to hit the plate remain constant.

Beam name	Properties				
	$E_{kin}$ GeV	$I$ $10^{13}$	$t_{bunch}$ $\mu s$	$t_{pulse}$ s	$\sigma_x, \sigma_y$ mm
ACCID	2	5	0.575	30	8.25, 6.09
HLLHC	2	2.4	0.575	30	4.42, 3.66
BCMS	2	1.6	0.575	30	3.51, 3.22
WORST CASE	2	2	0.575	30	3.51, 3.22

Table 3.2: PS beam properties for the design of new internal beam dumps.[41]

### 3.1.3. Energy Deposition

The energy deposition is computed by the FLUKA section at CERN. It is mapped throughout the plate with a resolution corresponding to the size of the volume elements (in FLUKA a volume element is also referred to as a bin). The energy deposition density is very high in the beam impact zone but relatively low outside it. Therefore the area outside of the impact zone can be relatively coarse so that the calculation power needed for simulations is reduced. So two spatial meshes were defined in FLUKA. A coarse map, where a bin sizing of 0.8 mm x 0.8 mm x 1 mm is used (figure 3.2.a), and a fine map that has a binning of 0.0833 mm x 0.0833 mm x 1 mm (figure 3.2.b). From figure 3.2b the energy deposition gradient is visualized much better. In ANSYS, the energy deposition density on a node is interpolated from the energy deposition values of the eight surrounding bins.

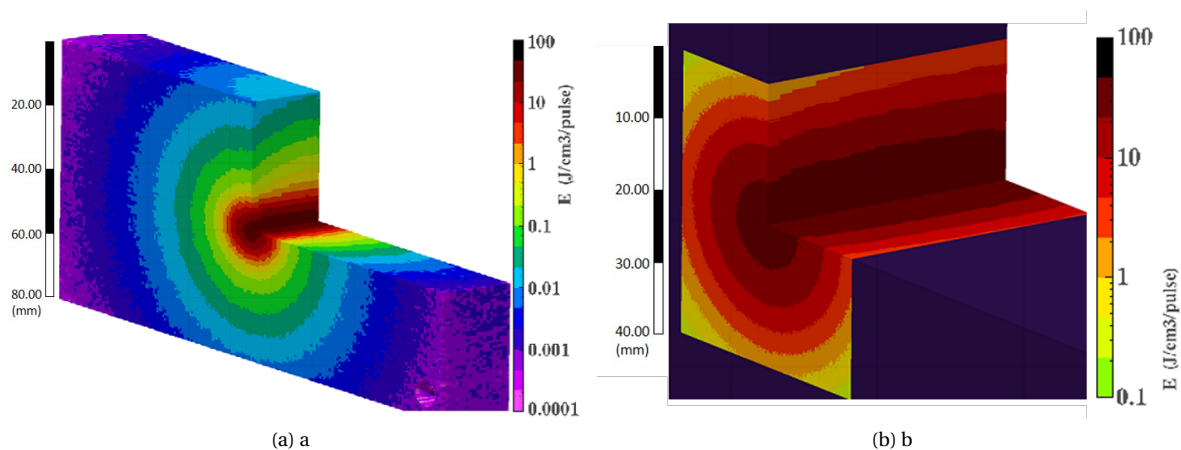


Figure 3.2: a: FLUKA energy deposition map for coarse binning. High Luminosity LHC beam and IT180.[44] b: FLUKA energy deposition map for fine binning. High Luminosity LHC beam and IT180. [44]

In figure 3.2a the energy deposition over the entire plate shows that for lower energy deposition areas, the colour transition is less sharply defined. This can be attributed to a lower energy deposition resulting in less particle data and therefore a larger statistical error. Additionally we can see that the colour transitions in the

coarse plot in the center are less sharply defined than the colour transition in the fine plot (figure 3.2b) which is due to the difference in resolution. From the fine plot the energy deposition gradient is sharply defined and it is easier to read the maximum of  $90 \text{ J/cm}^3/\text{pulse}$  per cm in the plot. Furthermore in the direction of the beam trajectory (from left to right) the energy deposition gradient decreases (larger circles) indicating as well the beam diverging. Due to interactions with matter, the protons are deflected from their path causing the beam to scatter as it travels through a medium.

Figure 3.3a shows the number of particles entering and exiting the plate. At the center of the plate, where  $X=0$  the beam is diluted from peak incoming particle density  $2.8 \times 10^{11}$  particles per  $\text{mm}^2$  to peak outgoing particle density  $2.6 \times 10^{11}$  particles per  $\text{mm}^2$  due to the scatter from plate impact. Where  $X > 5$  mm, we see that the particle density has increased showcasing the diverging effect the beam undergoes when the beam hits the tungsten plate.

Figure 3.3b shows the energy deposition of the worst case scenario of the incident beam versus the outgoing beams for both Tungsten and IT180. For the FLUKA application, all protons in the incident beam are assumed to be at 2 GeV in the middle of the machine acceptance energy range (approximately 1.98 GeV to 2.02 GeV, see figure 3.3b). If particles fall outside of the Proton Synchrotron Machine Acceptance energy range it means they have too little momentum to be further accelerated. The beam will continue several meters inside the machine after which it is 'lost', into the beam pipe wall and further losing energy through material interactions outside of the accelerator. The energy spectra of the beam exiting the plate for both materials are outside of machine acceptance and the SEM-grids being 20 meters away can be considered safe. The outgoing energy spectrum for Tungsten is slightly lower than that for IT180. This is in agreement with the expectation that a greater energy deposition occurs in tungsten due to its higher density and therefore increased particle interaction.

The maximum energy deposition in the tungsten plate, given by FLUKA is  $9.68 \times 10^{11} \text{ GeV/cm}^3$ .

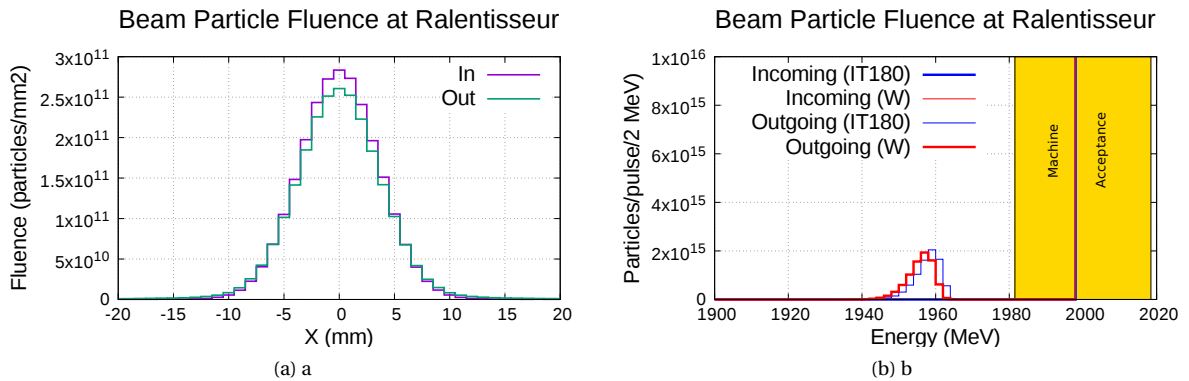


Figure 3.3: a: Worst case scenario fluence of the particles going into the Ralentsseur plate and coming out of the plate. [44] b: Energy spectra of proton beam particles incident and exciting the Ralentsseur in comparison with machine acceptance.[44]

### 3.2. Thermo-Mechanical Simulations in ANSYS

To study the thermally induced stresses in the Ralentsseur plate, finite element simulations are performed. In total 27 thermal and 15 structural simulations have been performed (see figure 3.4). Four different simulations are done:

1. **Thermal** simulations apply the FLUKA energy deposition data on the body mesh as defined in ANSYS. Where, combined with the material property model, the temperature evolution over the meshed plate body over time is computed.
2. **Structural** simulations load the transient temperature simulation results into another ANSYS module which uses the predetermined material model to calculate the local volume change. This deformation results in stresswaves. In the structural simulation, ANSYS uses the material model to compute these resulting thermal deformation and accompanying stresses over time.

3. **Steady State** simulations apply the FLUKA energy deposition continuously until the absolute heat loss is equal to the total energy deposition. This simulates the scenario where accidentally the Ralentisseur would receive beam continuously longer than foreseen. Since the steady state heat loss would have to equal the FLUKA energy deposition, this simulation also allows for verification of the heat loss boundary conditions.
4. **Energy check** simulations compare the energy deposition computed in FLUKA to the energy deposition applied on the mesh nodes in ANSYS. As FLUKA uses volume elements to calculate the data points, these values are interpolated to nodal data points and hence there is an error.

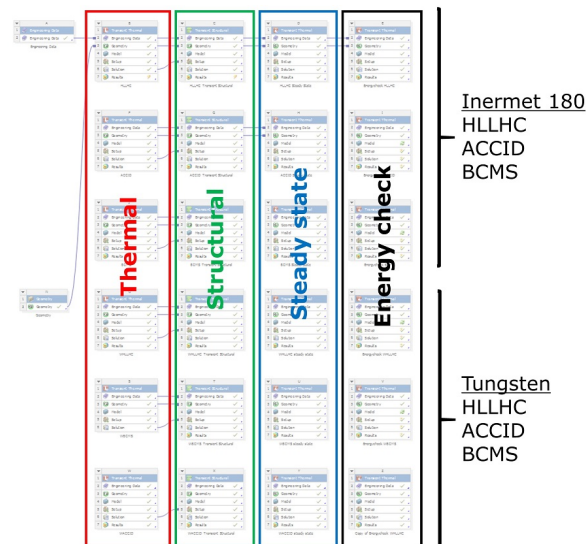


Figure 3.4: Overview of the Ralentisseur ANSYS project including all different modules for thermal, structural, steady state and energy-check simulations.

### 3.2.1. FLUKA Energy Deposition Data Application in ANSYS APDL

Connecting the FLUKA produced text file of energy deposition data points to our Thermo-Mechanical simulation in an ANSYS parametric design language script (from now on referred to as APDL). Based on CERN's best practice method [16] and adjusted for this specific problem J. Esala applied this method to perform thermo-mechanical simulations for the design of the new PS internal dump core [12] which consists of pressed fine grain graphite and a precipitation hardened alloy (CuCrZr) enduring a 150 ms interaction with a 26 GeV proton beam. A. Ouzia followed a similar approach to model a Graphite 160 MeV proton beam stopping block for the future LHC injector Linear Accelerator 4 [45]. Figure 3.5 shows the format of the heat load data which is imported into ANSYS. The units are converted to total Joule deposited per volume unit per pulse. The FLUKA values are located in the bin centers. In ANSYS the energy deposition should be applied to either a node or an element. If a bin center does not coincide with a node or element the nodal values are calculated by interpolating from surrounding bins. The APDL script then applies the nodal values on the node with the matching coordinates.

### 3.2.2. Boundary Conditions

Figure 3.7a shows the CAD model that was used to perform the FEM simulations. The model of the beam hitting the tungsten plate is symmetric in the XZ-plane and as shown in figure 3.7b symmetry is used the boundary conditions. By using symmetry boundary conditions only half of the plate is simulated and only half of the results are computed. Therefore the computation force needed is substantially reduced. Figure 3.6 shows the fixed nodes are far from the impact zone to minimize their impact on the results in the most critical areas. Regarding heat loss conduction and radiation are being considered. Reflected radiation from the vacuum vessel are not taken into account and convection is neglected because the plate is in a high vacuum. The interfaces where heat loss occurs are visible in figure 3.7a where the heat transfer occurs though



```

Start and end coordinates of
the volume in x direction
# of bin divisions
Bin size
Power deposition volume
data points in GeV/(cm³s)
Cartesian binning n. 1 "ENERGY-F ", generalized particle n. 208
X coordinate: from -8.0000E+00 to 8.0000E+00 cm, 200 bins ( 8.0000E-02 cm wide)
Y coordinate: from -4.0000E+00 to 4.0000E+00 cm, 100 bins ( 8.0000E-02 cm wide)
Z coordinate: from 0.0000E+00 to 2.0000E+00 cm, 20 bins ( 1.0000E-01 cm wide)
Data follow in a matrix A(ix,iy,iz), format (1(5x,1p,10(1x,e11.4)))

accurate deposition along the tracks requested
3.1543E-07 3.5554E-07 3.0876E-07 2.5658E-07 4.3954E-07 4.3996E-07 5.4306E-07 5.9007E-07 5.5690E-07 8.4854E-07
4.9676E-07 3.6628E-07 4.8572E-07 5.3217E-07 7.2410E-07 7.1030E-07 7.9214E-07 1.1554E-06 8.8524E-07 6.3110E-07
6.1956E-07 9.8290E-07 9.2290E-07 1.0457E-06 1.1811E-06 1.1733E-06 1.4119E-06 1.1839E-06 7.8996E-07 8.3824E-07
9.8637E-07 9.1113E-07 2.1520E-06 1.4626E-06 9.2153E-07 1.7040E-06 2.0969E-06 2.0629E-06 2.0205E-06 1.3102E-06
1.4319E-06 1.6055E-06 1.5056E-06 1.7188E-06 2.1586E-06 2.1474E-06 2.2947E-06 2.8235E-06 2.5170E-06 2.3305E-06
    
```

Figure 3.5: Example of FLUKA data file for ANSYS energy deposition input. [44]

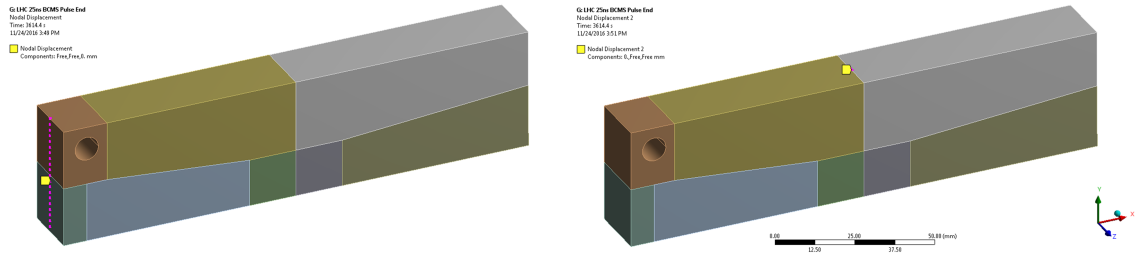


Figure 3.6: The fixed nodes in the simulation are a line of nodes in the center on the side and one single node on the top.

conduction in the pinhole and through radiation on the exposed surface. Section 3.3.2 of the Master thesis on the design of the PS dump core [12] exactly describes the formulas behind the heat loss as it is applied in ANSYS.

The two different FLUKA energy deposition maps shown in figure 3.2a and 3.2b are applied in ANSYS so an energy is deposited on the body like a load. The coarse map is only applied to the plate outside the beam impact zone and the energy deposition map with a higher resolution is applied as a load to the beam impact region.

### 3.2.3. Mesh

The area of the plate where the beam impacts, the impact zone, undergoes very dense energy deposition. That is why this area needs a much finer mesh than the surrounding material. For computing a finer mesh in the beam impact area, the 3D body of the plate is sectioned (figure 3.7b). To reduce calculation time the mesh outside of the beam impact area is much coarser. The FLUKA energy deposition resolution is 0.8 mm x 0.8 mm x 1 mm for the coarse part and 0.0833 mm x 0.0833 mm x 1 mm for the refined part but using this as mesh size would result into an excessive amount of elements and long computation times. Therefore the outside (figure 3.7b) mesh has coarse edge sizing of 2 mm and fine edge sizing of .4 and .5 mm.

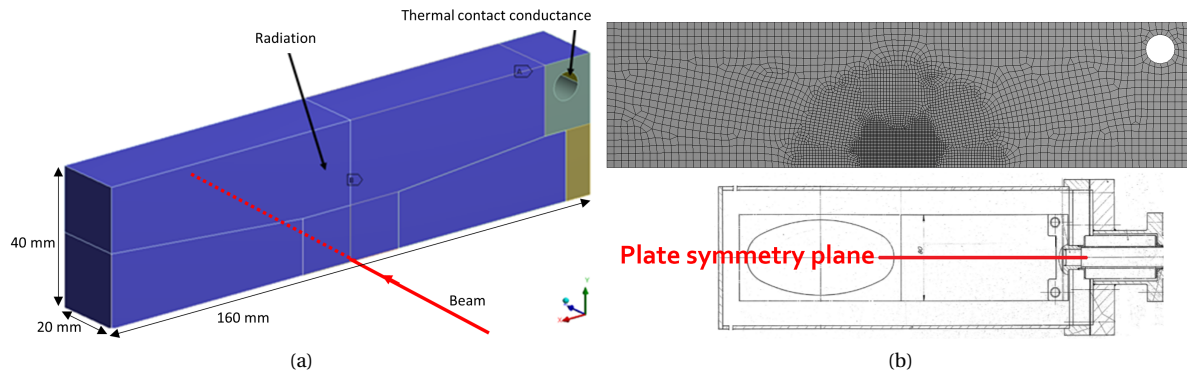


Figure 3.7: a: Top half of plate sectioned with radiation and conduction boundary conditions applied. b: Plate mesh of half the plate. A symmetry is assumed over the center xz-plane and the mesh remains constant throughout the thickness of the body.



### 3.2.4. Simulation Reliability

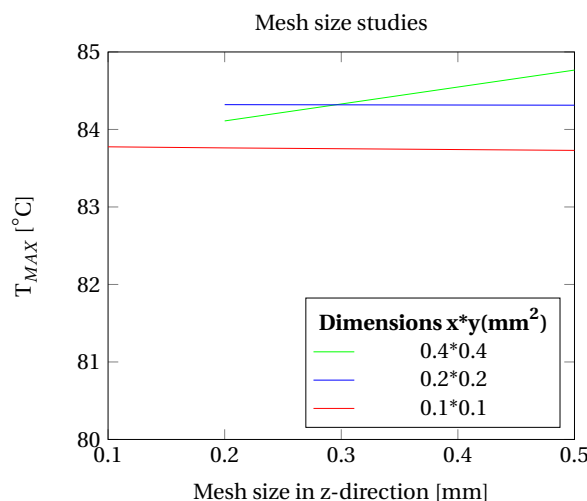
To verify the model several checks are performed. For future work a best practice quality checklist [46] was made and presented during the ANSYS simulation forum at CERN. To check whether the boundary conditions were applied accurately the following points are discussed: Beam Parameters, Material Data, Geometry, Contacts, FLUKA to ANSYS data import, analysis setting, mesh and post processing.

To see whether the FLUKA load file was imported into ANSYS and applied to the model correctly, an extra simulation is performed. A dedicated ANSYS model checks whether the energy deposition (as discussed in section 3.1.3) in the FLUKA file coincides with what is computed in the ANSYS model. For the FLUKA file as well as for the ANSYS model, the total deposited energy and the peak deposited energy are calculated. The error for the total deposited energy is 0.02% and the error for the peak deposited energy density is 0.1% (see table 3.3) which is an acceptable precision [12]. This error can be explained by the fact that the energy deposition is a point value in the center of the bin. The nodal value does not always coincide with a bin center and in that case is interpolated from the bin center values surrounding the node. This interpolation creates an error. The total energy deposition also confirms that a higher amount of energy deposition and thus interaction occurs in tungsten, as expected due to its higher density.

		FLUKA	ANSYS	Error[%]
<b>Total deposited energy</b>				
Tungsten	[J]	390.5	390.7	-0.051
IT180	[J]	419.6	419.8	0.040
<b>Peak deposited power (density)</b>				
Tungsten	[J/cm <sup>3</sup> ]	147.9	147.7	-0.088
IT180	[J/cm <sup>3</sup> ]	158.7	158.4	-0.2

Table 3.3: Relative errors between FLUKA and ANSYS energy and power deposition for both tungsten and IT180.

To investigate whether the results would benefit from further mesh refinement, a separate set of simulations with the HLLHC beam impacting IT180 was performed. Two further refinements in x- and y-direction and two further refinements in z-direction were performed separately (see figure 3.8a). No dramatic changes in maximum temperature were found and so the mesh is assumed to be fine enough.



(a)

Figure 3.8: Mesh convergence studies results. The maximum temperature varying over mesh size.

Additionally, the model results were compared to a former ANSYS model of the current Ralentsisseur (tungsten). The current beams were used to simulate the current scenario with the model by Esala et al. [47] and

the model presented in this work. Both models give similar results. The models simulated the thermal and stress results with the same FLUKA files that were used by Esala et al. [47] and computed  $T_{max}=819\text{ }^{\circ}\text{C}$  and  $\sigma_{max}=44\text{ MPa}$ . Comparing these values to the values in the model by Esala et al. [47] ( $T_{max}=800\text{ }^{\circ}\text{C}$  and  $\sigma_{max}=44.8\text{ MPa}$ ), the values from the model presented in this report show strong similarity thus further validates the model. [47]

### 3.3. ANSYS Results

Table 3.4 gives an overview of the thermo-mechanical results for the different simulations. The maximum temperature after one pulse is barely different in Tungsten and Inermet180. However, the steady state temperatures vary somewhat. This is obviously driven by the difference in thermal conductivity, specific heat and density. But there is also different energy deposition caused by different beam interactions with the two different materials. The peak energy deposition in Tungsten is higher than the peak energy deposition in Inermet 180. Regarding the difference in stresses, despite the Inermet 180 Young's modulus being lower than the Young's modulus for tungsten, higher thermal stresses are achieved for Inermet 180. Regardless, the stresses are too low for yield to occur. Since the temperatures of all beam impacts remain well below the maximum operation temperatures and the resulting stresses remain below the yield stresses simulations and results are very similar (see table 4), only the simulation results for HLLHC and Inermet180 are discussed.

	Inermet 180	Tungsten
	HLLHC	
$T_{max}[^{\circ}\text{C}]$	84 (t=0.6 $\mu\text{s}$ )	84 (t=0.6 $\mu\text{s}$ )
$T_{max,analytical}[^{\circ}\text{C}]$	87	87
$T_{steadystate}[^{\circ}\text{C}]$	294(t=43200s)	304(t=43200s)
$\sigma_{VonMises,max}[\text{MPa}]$	116(t=0.8 $\mu\text{s}$ )	107 (t=0.8 $\mu\text{s}$ )
	ACCID	
$T_{max}[^{\circ}\text{C}]$	70 (t=0.6 $\mu\text{s}$ )	69 (t=0.6 $\mu\text{s}$ )
$T_{max,analytical}[^{\circ}\text{C}]$	73	73
$T_{steadystate}[^{\circ}\text{C}]$	417(t=43200s)	430(t=43200s)
$\sigma_{VonMises,max}[\text{MPa}]$	145(t = 4.8 $\mu\text{s}$ )	135(t = 4.0 $\mu\text{s}$ )
	BCMS	
$T_{max}[^{\circ}\text{C}]$	79 (t=0.6 $\mu\text{s}$ )	79 (t=0.6 $\mu\text{s}$ )
$T_{max,analytical}[^{\circ}\text{C}]$	82	82
$T_{steadystate}[^{\circ}\text{C}]$	235(t=43200s)	243(t=43200s)
$\sigma_{VonMises,max}[\text{MPa}]$	105(t=0.7 $\mu\text{s}$ )	97 (t=0.7 $\mu\text{s}$ )

Table 3.4: An overview of the results for the thermal, structural and steady state simulations for all beams and including the analytically derived adiabatic predictions.

#### 3.3.1. Thermal Simulations

In the thermal simulations, radiation takes place over the plate surface and conduction occurs through the supporting pins. The temperature rises and at the end of the beam pulse (0.6  $\mu\text{s}$ ) the maximum temperature of 84  $^{\circ}\text{C}$  is achieved (see figure 3.10). The energy deposition is not precisely symmetric in the middle XY-plane of the plate and as a result the temperature distribution is not exactly symmetric through the center of the tungsten plate. Instead there is a higher energy deposition in the part where the beam is exiting the plate, which is also coherent with the FLUKA result in figure 3.2a. Finally, the heat generation occurs in a short time (see figure 3.9a), very locally. In 0.6  $\mu\text{s}$  the maximum temperature is reached in a small region with a radial temperature gradient of about 60  $^{\circ}\text{C}$  in x- and y-direction. This will cause localized and rapid thermal expansion which will be further discussed in section 3.3.3. The temperatures are too low to contribute to annealing of any induced radiation damage [48].

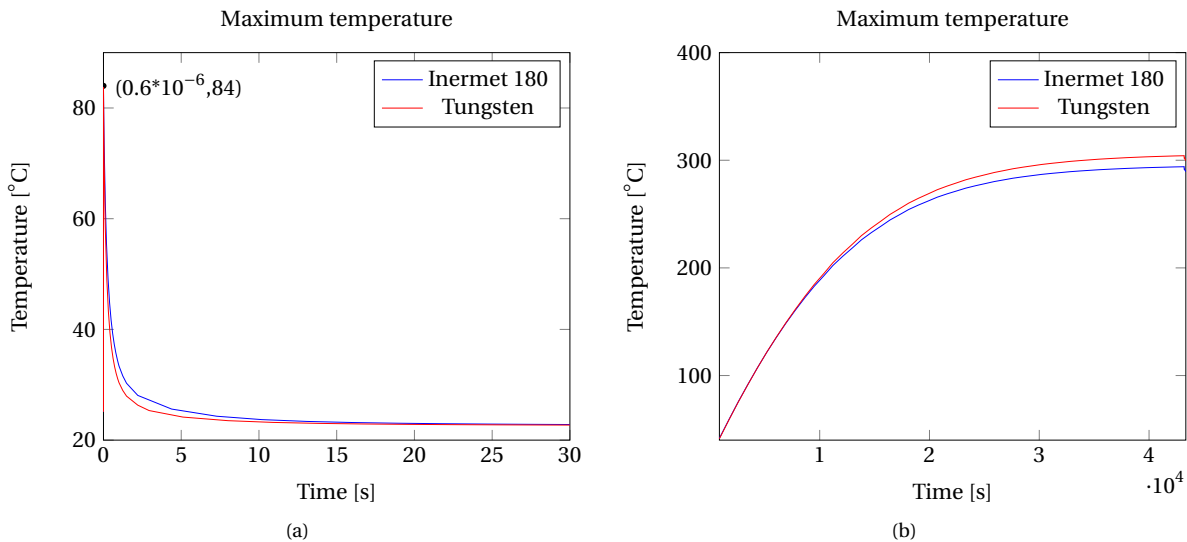


Figure 3.9: a: Maximum temperature from a single HLLHC pulse beam interaction. b: Steady state temperature from a single HLLHC pulse beam interaction.

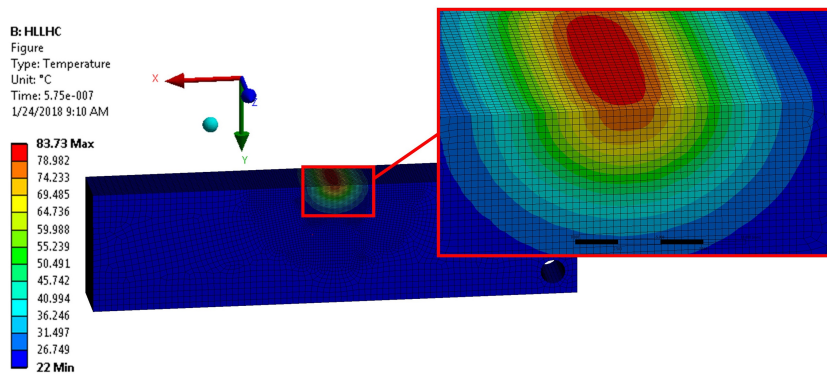


Figure 3.10: Inermet 180 thermal transient simulation of a single HLLHC beam pulse interaction.

### 3.3.2. Steady State

In the steady state simulation, a pulse consisting of a single bunch is applied every 30 seconds until steady state is achieved (figure 3.11). Even if this event were to accidentally occur, the temperatures on the plate remain uncritical (see table 3.4). Utilizing a reaction probe, the heat loss through radiation on the surface (5.4 W) and the heat loss through conduction in the pin hole (1.3 W) over half the plate are measured. The total heat loss over the entire plate would therefore be 13.4 W, which also coincides with the energy check simulation where the total energy deposition of the FLUKA file is calculated. Furthermore the temperatures are far below maximum working temperature and indicate there is no need for additional cooling of the plate.

### 3.3.3. Structural

As mentioned in section 3.3.1, the highly localized energy deposition causes a relatively large temperature gradient around the beam impact area. The instantaneous temperature increase in the center causes a thermal expansion and centralized compression surrounded by material at room temperature translating into a stress wave throughout the material (figure 3.12a). In IT180, some time after the maximum temperature, the maximum stress is achieved (figure 3.14). There are compressive stresses throughout the center and tensile stresses on the surface. The maximum stresses are compressive stresses in the center (figure 3.12b). In figure 3.13b, stresswaves can be seen propagating throughout the material. For pure tungsten, the maximum and minimum principal stresses are plotted and directional tensile stresses throughout the material also show stresswaves (figure 3.13a and 3.13b). These stresses can be used to evaluate the fatigue limit for the plate.

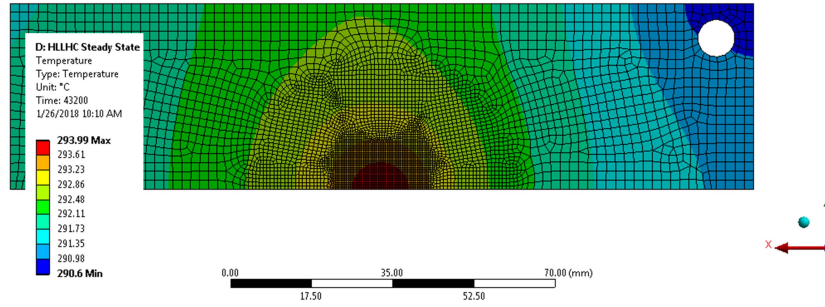


Figure 3.11: Thermal transient simulation of continuous beam pulse interactions until steady state is reached.

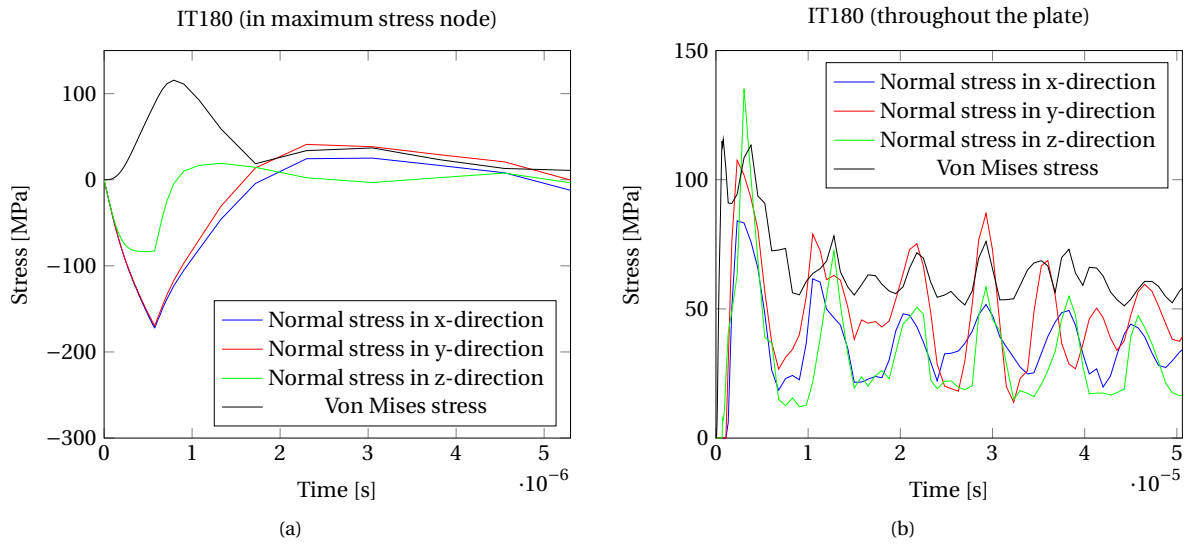


Figure 3.12: a: Directional and equivalent Von Mises stresses in the node with the most critical stresses from a single HLLHC pulse beam interaction. b: Tensile stresses and Von Mises Stress in Inertmet 180 from a single HLLHC pulse beam interaction.

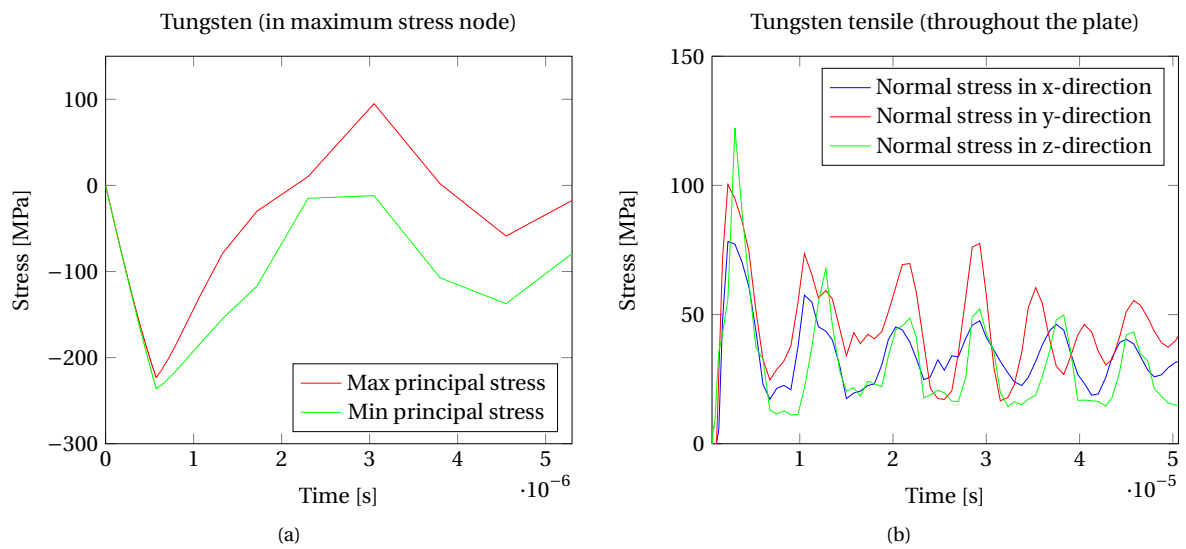


Figure 3.13: a: Minimum and Maximum Principal stresses in pure tungsten from a single HLLHC pulse beam interaction. b: Tensile stresses in pure tungsten from a single HLLHC pulse beam interaction.

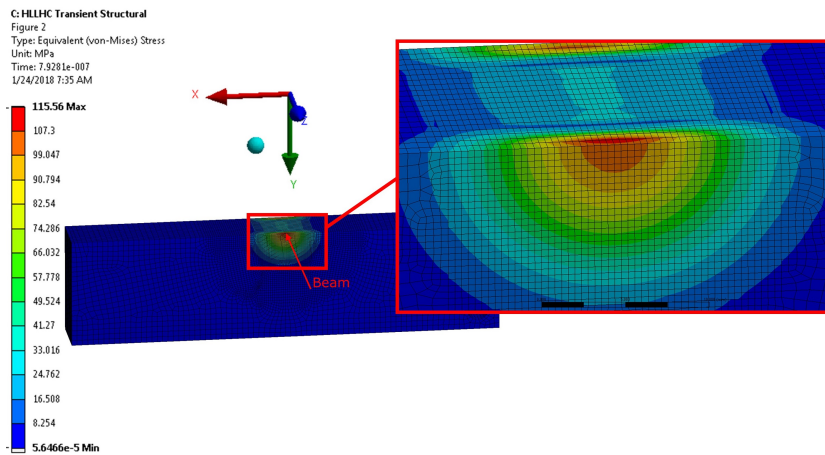


Figure 3.14: The Von Mises Stresses for the HLLHC beam interaction with Inermet 180 at  $\sigma_{max}$ .

### 3.4. Discussion

The interactions of the current Ralentsisseur geometry with three LIU beams and one 'unforeseen' worst case scenario beam were evaluated for two different materials. A 20 mm thick plate of pure W or Inermet stops 20% of the beam intensity at 2 GeV and the remaining particles do not have enough energy to make another turn in the PS Machine. Having that information, the actual design (presently installed in the PS Machine) is compliant with the functional SEM grids protection requirements for LIU beams. The Ralentsisseur's mechanical and physical integrity needs to be maintained. Using FLUKA energy deposition maps with FEM software, thermal transient and structural transient simulations were performed. The resulting temperatures remained well below critical values. The Von Mises stresses remain below yield stress, indicating that no plastic deformation will take place. Considering the temperatures reached in the thermal simulations, the change in density due to thermal expansion is not significant for the device lifetime. However, if a significant change in temperature is reached, the Monte Carlo simulations should be redone with appropriately adjusted densities.

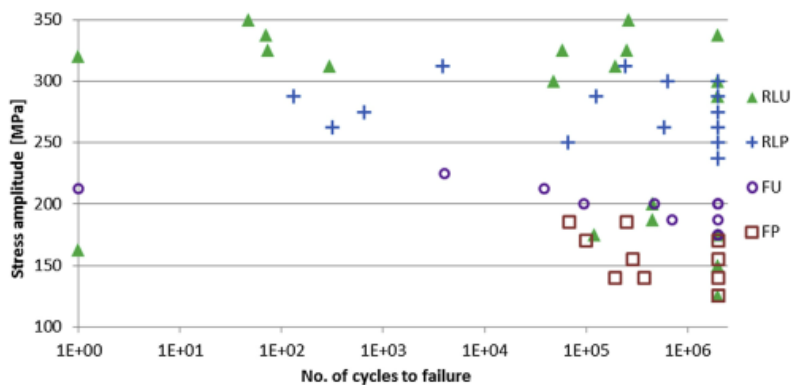


Figure 3.15: Wohler diagram for rolled and forged tungsten at 25 °C. [49]

However, the European Spallation Source conducted fatigue research for both IT180 and several grades of pure tungsten. Working at very similar energy levels, stresses and temperatures, a wohler diagram for different grades of tungsten was composed (see figure 3.15). RLU stands for rolled unpolished, RLP stands for rolled polished, FU stands for forged unpolished and FP stands for forged polished. The wohler diagram shows a large spread due to the materials' brittle nature. Since the results remain above a stress amplitude of 100 MPa, a rule of thumb that is handled is that for a brittle material such as pure tungsten, all principal stresses should remain below 100 MPa. (personal communication with J. Descarrega) To cope with the stresses the Ralentsisseur material shall be more ductile. The much more ductile Tungsten heavy metal alloy

Inermet 180 is a good candidate.

Additionally, verification models were performed as well as thermal simulations where beam interaction until steady state is computed. The verification models confirmed that the same amount of power was applied to the ANSYS model as was computed by ANSYS. Furthermore, the heat loss at steady state can be considered small enough so no cooling is needed. Finally a comparison between the FEM results for all beams was made where the thermal transient simulations are analytically verified and the thermal and stress simulations were cross checked with previous simulations. For operation with the most critical beam, there is a factor 10 between the maximum temperatures and the maximum working temperatures and a factor 5 regarding stress and yield strength. Either tungsten or Inermet would be appropriate for the functionality, but Inermet is easier to machine. Based on the calculations performed for the HL-LHC beam (see table 3.4), the proposed conceptual design maximum operational limit is:

- A beam with a momentum at injection of 2 GeV/C
- An intensity of  $2 \times 10^{13}$  protons per pulse
- A pulse length is 0.575  $\mu$ s.
- A pulse period 30 s
- Pulsing can occur continuously until steady state.

At steady state, the maximum temperature can reach up to 300°C (HL-LHC, considering an intensity of  $2.4 \times 10^{13}$ ) where temperatures remain below operational limits. These conditions can be considered to be the operation limits for which the Ralentisseur can perform.

## Radiation Damage Simulation and Results

The proton beams described in the previous chapter result in radiation damage. Radiation damage effects are the formation of defects such as vacancies, interstitials, dislocations, dislocation loops, voids and bubbles. These defects affect physical and mechanical material properties and can cause unforeseen failure. A major influence to the formation and behavior of these defects due to radiation damage are the production of DPAs. These DPAs are created during ion tunneling, sub-cascade and thermal spikes (explained in section 2.1). Besides DPAs, H and He are formed through transmutation and further induce microstructural changes. To estimate the DPA, H and He production in the Ralentisseur plate, the impact of a proton-beam with the tungsten plate is simulated using FLUKA. Figure 4.1 shows the proton distribution within the beam with the beam parameters as given in table 3.2) for HLLHC beam. In this chapter the DPA, H and He production resulting from the impact is calculated. The results are presented and their implications on material properties are discussed.

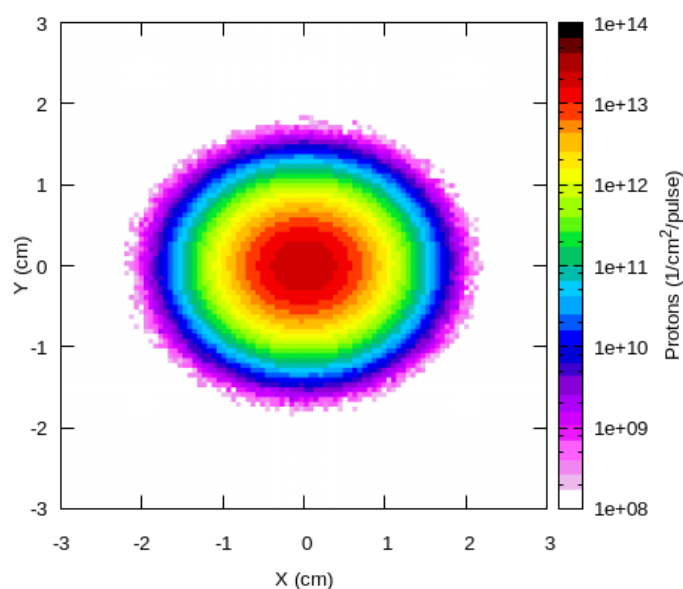


Figure 4.1: HLLHC-beam proton distribution used to calculate DPA, H and He production.

## 4.1. Preliminary Study

For the case of the Ralentisseur, temperatures remain relatively low ( $T/T_m < 0.35$ ). Ullmaier et al. [50] summarizes radiation damage effects and the underlying physical processes. From the ranges of radiation damage effects on figure 4.2 it is clear that the main focus should lie with the radiation induced hardening and hydrogen embrittlement effects. Irradiation hardening mainly affects the yields stress. The UTS and work hardening coefficient are much less affected. This is also confirmed by the experimental data achieved by Maloy et al. Figure 2.11b shows a considerable increase of Yield strength however, the UTS and hardening coefficient are much less affected. Ullmaier explains that irradiation hardening in BCC metals is dependent on multiple factors. Firstly, alloying elements even minor can have a large influence. Secondly, screw dislocations in BCC metals are quite immobile, contributing significantly to hardening at lower temperatures. This also influences the ductile to brittle transition temperature to increase for lower temperature or increased dose irradiation.

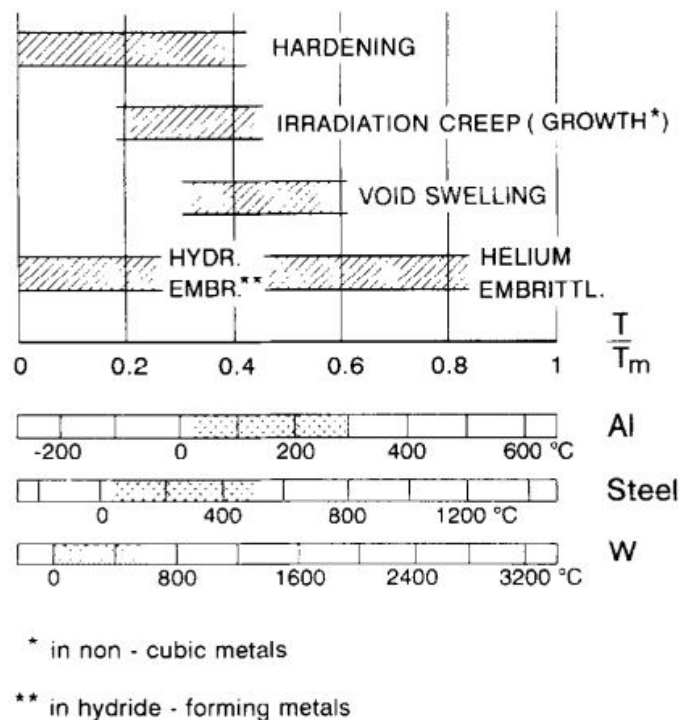


Figure 4.2: Approximate range of temperatures (normalized to the melting point  $T_m$ ) where the radiation-damage effects described in the section on Changes of Macroscopic Properties occur. Irradiation growth is restricted to noncubic metals. Hydrogen embrittlement is expected only for cases with extremely high production rates for hydrogen isotopes such as in spallation target materials. [50]

### 4.1.1. Microstructure Evolution With Cascades

Point defects created from cascades can either annihilate, become immobile through sink formation and interaction or long range migration can occur. The proportions of these three events is influenced by the size and shape of the cascades. During the "cool down" period, vacancies form agglomerates which eventually disintegrate into vacancy loops or stacking fault tetrahedra. As explained in section 2.1, vacancies are much less mobile than interstitials the interstitials can travel much further than the vacancies. After the initial recombination of Frenkel pairs, the concentration of interstitials will much sooner drop due to interaction with defects such as grainboundaries and dislocations. Therefore the amount of vacancies is higher than the number of interstitials. After the cool down period in the Ralentisseur, temperatures during normal operation remain relatively low. Too low for further annealing to occur. The remaining radiation damage can also interact with transmutation elements in the lattice.



### 4.1.2. FLUKA Monte Carlo Simulations

To gain more insight on the radiation damage production and transmutation into helium and hydrogen, beam-material interaction is simulated using FLUKA Monte Carlo code. FLUKA is a general purpose Monte Carlo radiation transport code that computes the transport through matter for over 60 particles and heavy ions over an energy range of 1 keV to 1000 TeV. The models used and the extensive benchmarking are well explained by Battistoni et al. [51, 52, 53]. For the purpose of the work presented in this thesis, the interaction of a single proton with a homogeneous, isotropic material is computed. Existing imperfections in a lattice, grain-boundaries and defects created by earlier proton impact are not accounted for. Unless low energy neutrons are evaluated, changes in temperature due to energy deposition are not taken into account.

It tracks the following interactions:

- Hadron-nucleus interactions
- Nucleus-Nucleus interactions
- Electron interactions
- Photon interactions
- Muon interactions (inc. photonuclear)
- Neutrino interactions Decay
- Low energy neutrons
- Ionization
- Multiple scattering
- Combinatorial geometry
- Voxel geometry
- Magnetic field
- Analogue or biased
- On-line buildup and evolution of induced radioactivity and dose

### 4.1.3. Computing the DPA Production in FLUKA

A detailed explanation of modeling radiation damage using FLUKA is given by Briz et al. [54] of which a brief summary is given below: The radiation damage in an irradiated crystal structure is measured in displacement per atom (DPA), an average number of times every atom in the material was displaced. It is described by equation 4.1

$$N_{DPA} = \frac{A}{N_A \rho} N_F \quad (4.1)$$

Where  $N_{DPA}$  is the produced DPA density,  $A$  is the mass number,  $N_A$  Avogadro number,  $\rho$  the density and  $N_F$  the density of produced Frenkel pairs. Equation 4.2 shows the relation for the production of Frenkel pairs which depends on the threshold displacement energy  $E_{th}$ , a value that is dependent on direction but in literature the average for Tungsten is often calculated and defined as 90 eV. [55]

$$N_F = \kappa \frac{\xi(T) E_{kin,PKA}}{2E_{th}} \quad (4.2)$$

Where:

$\kappa = 0.8$  the displacement efficiency [56]

$\xi(T)$  = partition function (LSS theory) [57]

$E_{kin,PKA}$  = kinetic energy of the primary knock on atom

The Lindhard partition function is a physical approach to determine the fraction of stopping power that goes into non ionizing energy losses (interaction with nuclei). The Stoller results [56] originate from molecular dynamics simulations. Figure 4.3 shows a 6 GeV proton travelling through liquid argon. From the image it is clear that the proton travels some distance before it creates a PKA and also that further subcascades are created and the energy is dissipated into the liquid through multiple processes.

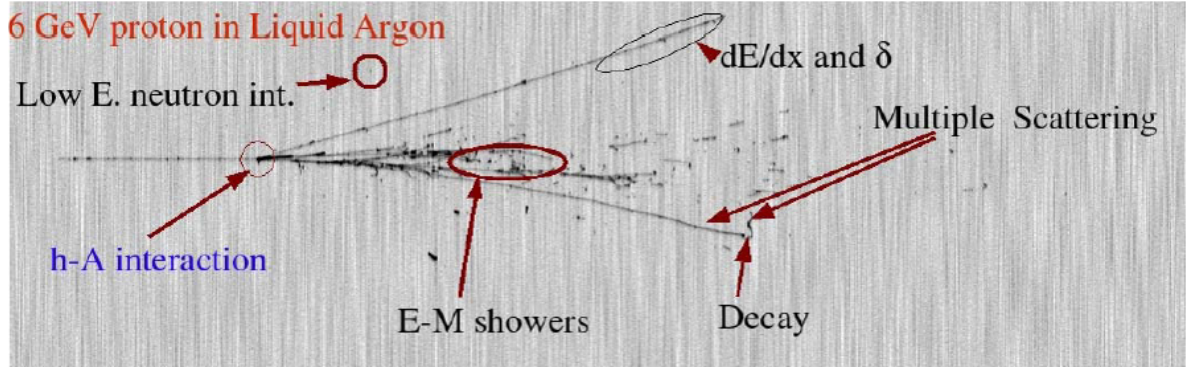


Figure 4.3: A proton travelling through liquid Argon and created particle showers and cascades from interaction.[54]

The production of DPAs and the transmutation that results in H and He atoms may be calculated as follows:

$$P_{DPA} = \phi_p \cdot \sigma_{DPA,p} + \phi_n \cdot \sigma_{DPA,n} \quad (4.3)$$

$$P_{He} = \phi_p \cdot \sigma_{He,p} + \phi_n \cdot \sigma_{He,n} \quad (4.4)$$

$$P_H = \phi_p \cdot \sigma_{H,p} + \phi_n \cdot \sigma_{H,n} \quad (4.5)$$

Where  $P_i$  is the production of a particle  $i$  per second,  $\phi$  is the flux per second and  $\sigma_{i,j}$  is the cross sections of a particle  $i$  being created from the interaction  $j$ . A cross section is the statistical chance that a specified particle interaction will occur.

## 4.2. DPA and Gas Calculations

The calculated results below are integrated values over the device lifetime for beam parameters as they are given in section 3.1.2. The foreseen use is a total of 4 weeks of commissioning and 15 years of 1 week of operation per year and an expected interaction with  $2 \cdot 10^{12}$  protons per pulse every 30 seconds which makes the following proton on target (POT) per lifetime:

$$intensity \cdot totalusageinweeks \cdot amountofprotonspersweek = 2 \cdot 10^{12} \cdot (15+4) \cdot 2 \cdot 60 \cdot 24 \cdot 7 = 7.66 \cdot 10^{17} \quad (4.6)$$

This is much less compared to the  $2 \cdot 10^{20}$  450 GeV protons on the SHiP target in section 2.3.1. The SHiP target already showed very low DPA values (0.9 for TZM and 0.7 for tungsten) and so the expectation would be to achieve even lower DPA and gas values in the Ralentsisseur. For the SHiP target, the maximum DPA is plotted to investigate whether significant changes of material properties will occur. However, the maximum gas production was plotted over penetration depth and both the distribution of gas and the distribution of DPA is not given. To evaluate the effects on material properties, it would be beneficial to also investigate the DPA and gas production distribution. Then besides separately evaluating maximum gas and DPA production values, the behavior of the radiation damage together with the gas elements could be evaluated. Ogorodnikova et al. evaluates the influence of radiation damage on plasma-induced deuterium retention in self-implanted tungsten. [55]

### 4.2.1. Tungsten

Figure 4.5a shows the XY-projection of the maximum DPA production. The maximum, shown in figure 4.4a, 0.0035 DPA is a relatively low value. The DPA produced per proton is quite low compared to values recorded for the ESS target studies where the expected fluence is  $5 \cdot 10^{22} \text{ cm}^{-2}$  over the course of its lifetime and the maximum calculated DPA is 12.4. This would make  $2.48 \cdot 10^{-22}$  DPA per proton where the above values amount to  $3.9 \cdot 10^{-21}$ . A lower amount of DPA per proton could be due to several factors. For example the beam shape is a major factor in DPA production or different material models could be used. But simulation results especially for these high energies also tend to vary when different codes are being used. This is because when taking into account the physical mechanisms different codes are making different assumptions. When adjusted for the much higher POT's in the SHiP target, the order of magnitude compares to the amount of

DPA that is produced in the SHiP target (see section 2.3.1). However, with the available experimental data for higher DPA values from Maloy et al. [38] these values are too low to give an estimation of the change of mechanical properties. These results would however be very suitable to study the by plotting the DPA and gas production over time. For these simulations the total beam interaction over the Ralenticisseur lifetime is plotted. With the distribution of the DPA and gas production over time the influence on further gas and DPA production on the mobility of DPA and gas could be investigated using diffusion models. Since the increase in defect and gas concentrations over time would result in new diffusion rates the rate of structural change in the material also changes. Structural changes affect cascade development of new incoming particles but in FLUKA structural changes are not taken into account when a new cascade is computed. At least in cases where densities change considerably, new FLUKA calculations, taking into account the change in density, can result in more accurate and precise values of DPA and gas production. The change in production of DPAs per proton requires iterations with new densities.

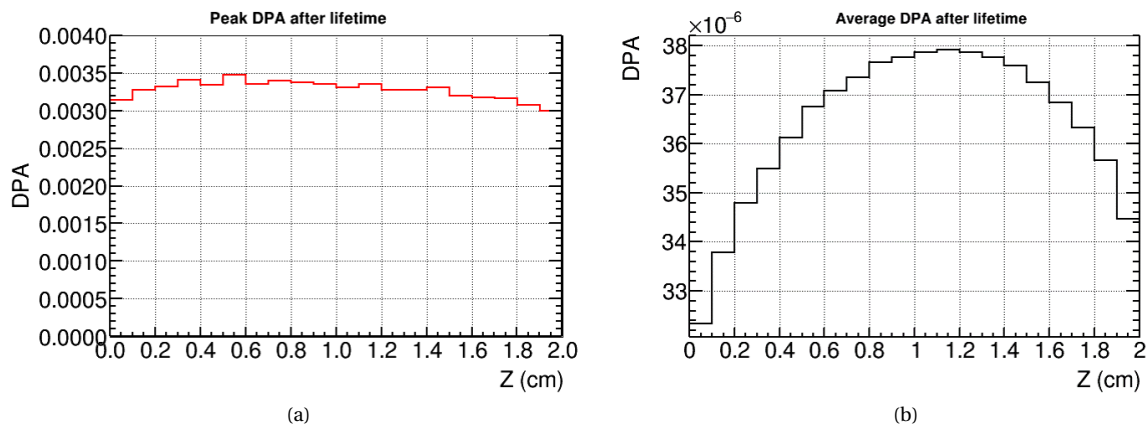


Figure 4.4: The average (a) and peak (b) DPA throughout the 2 cm thick tungsten plate. The beam enters the plate at 0.

Figure 4.4a shows the maximum, 0.0035 DPA, around  $Z=0.6$  cm which gives the highest concentration of DPA. Though from 4.4b the highest average DPA shows there is a larger area with lower maximum DPA values but higher DPA integrated over the  $xy$ -plane around  $Z=1.2$  cm. The DPA production from scattering is thus higher than the DPA production from the initial beam. This can be explained with cascade evolution. The initial protons create high energy PKA's that have low cross sections and therefore little interaction with ions on its path. Most of the interactions at this point are through coulombic interaction. After some time the PKA has lost a substantial amount of energy so that its cross section increases and the energy loss is dominated through interactions with surrounding ions. This explains why the maximum average DPA in figure 4.4b does not occur on the surface but in the bulk of the material.

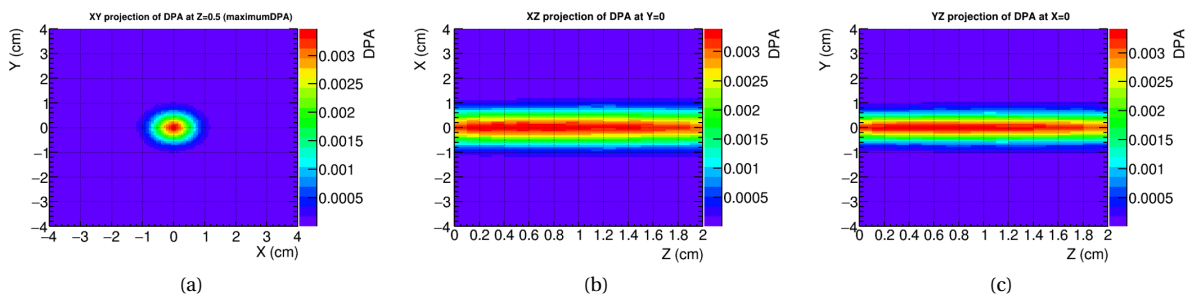


Figure 4.5: The DPA production over the lifetime of the Ralenticisseur in the a: XY b: XZ and c: YZ plane.

The cross section of DPA production area in the maximum  $xy$ -projection is larger than the cross section of the beam (see figure 4.5a). This is explained by scattering. The difference in the  $yz$ - and  $xz$ -projection still shows the beam shape where  $\sigma_x$  is larger than  $\sigma_y$ . Compared to the entire plate geometry, the DPA production

is limited to the center. This indicates that the high energy PKA's do not travel far. From the average DPA it is clear that a peak occurs just after traversing the center and so the high energy cascade components create defects no further than 1 cm from the center. Even though it may seem that the cascade is contained to the central area, beam-material interaction goes beyond the creation of defects and so it does also affect the surrounding environment. Even though it is beyond the scope of radiation damage in materials, what is also an important factor in choosing a material is how its interaction with the beam affects surrounding equipment. Simulations to calculate the dose to the surroundings were done. Figure 4.6 shows the dose to surrounding equipment, a magnet and the Ralentsisseur actuation system. Geometries have been simplified to 'boxes' and 'cylinders' in order to comply with computation force availability.

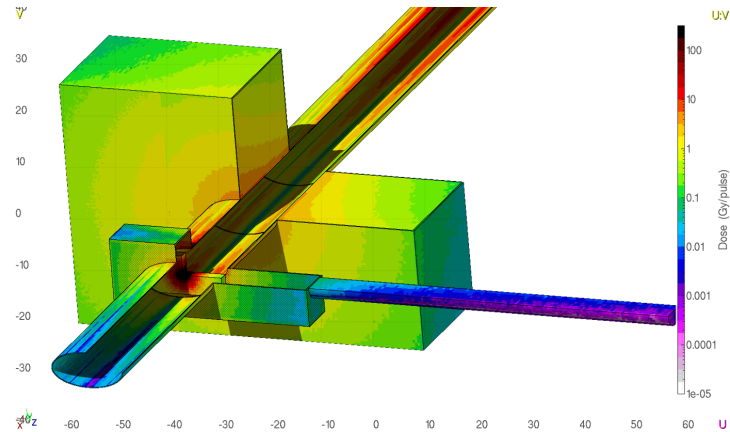


Figure 4.6: The dose (in Grey per pulse) on equipment surrounding the Ralentsisseur. (courtesy of J. Briz Monago)

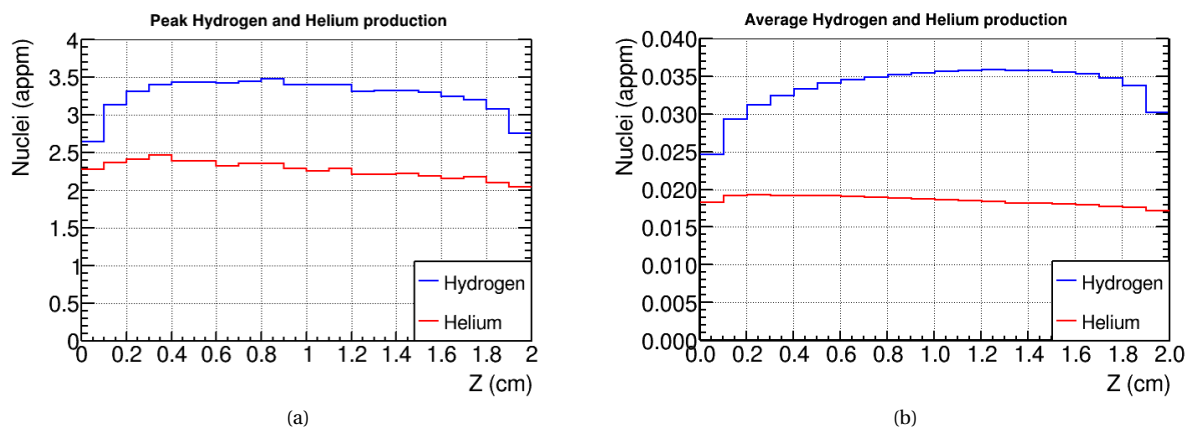


Figure 4.7: The average (a) and peak (b) hydrogen and helium gas throughout the 2 cm thick tungsten plate. The beam enters the plate at 0.

Figure 4.7a and 4.7b give the peak and average hydrogen and helium production throughout the plate XY cross section. The peak He production (2.5 appm) occurs closer to the plate surface around 0.4 cm whereas the peak H production (3.5 appm) occurs after further scattering around 0.8 cm. The highest average of He and H occur around 1.2 and 0.2 cm. Like in other literature, the amount of H produced is substantially higher than the amount of He produced. This is in coherence with calculations of H and He production from 2 GeV proton-tungsten interactions at these temperatures [40]. It is also clear that the average gas production throughout the plate is more constant than the average DPA production. Where the average helium production remains most constant. As expected from the SHiP target design gas production calculations, the amount of helium and hydrogen produced is very low. Like the DPA values, when adjusted for the much higher POT's in the SHiP target, the order of magnitude compares to the amount of gas that is produced in the SHiP target.

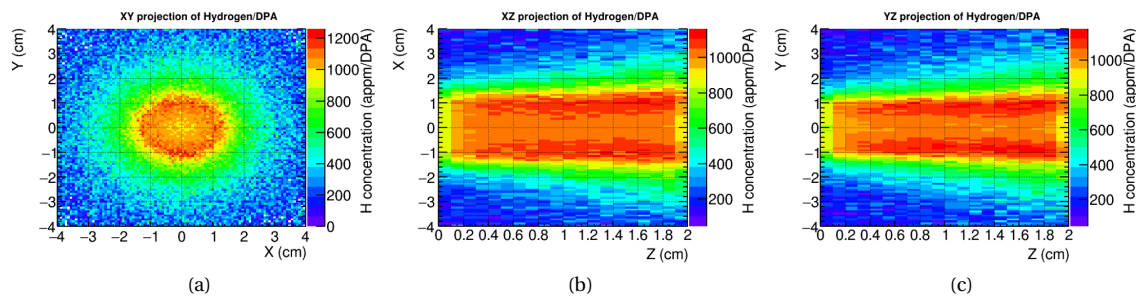


Figure 4.8: The hydrogen production over the lifetime of the Ralentsisseur in the a: XY b: XZ and c: YZ plane.

Figure 4.8a, 4.8b and 4.8c show the distribution of hydrogen, normalized with radiation damage, in the xy-, xz- and yz-plane. Figure 4.8a shows that the peak H/DPA occurs in a ring around the center of beam impact. And throughout the plate thickness, the peak H production does not occur in the center of the beam (see figure 4.8b and 4.8c). The maximum, 1270 appm/DPA compares to the values that were achieved in similar simulations of the European Spallation source discussed in section 2.3.4, namely 850 appm/DPA. An important difference there, is that much higher levels of DPA and hydrogen were calculated and so it is possible that after a certain amount of hydrogen production further transmutation occurs where the hydrogen produced in the center is consumed or that the H reacts with the radiation damage. Investigating the evolution of the H, He and DPA production distribution in tungsten would give insight into further transmutation. To evaluate gas and defect mobility and to investigate the formation and behavior of 2D and 3D defects with point defects, gas atoms and other transmutation elements, diffusion models can be used. For example the influence of radiation damage on plasma induced deuterium retention in self-implanted tungsten was investigated by Ogorodnikova et al. [55] Two 99.95 wt% purity tungsten samples from different suppliers and with different grain size were outgassed and self implanted with 5-20 MeV tungsten ions at 290 K. To separate deuterium retention in plasma induced traps from deuterium retention in displacement damage created by the tungsten ions, the samples were implanted with Deuterium on both the irradiated and unirradiated side. The results gave more insight on deuterium diffusion in tungsten, the rate at which vacancies and vacancy clusters are filled was found and a relation for He+D and pure D with depth was derived [55].

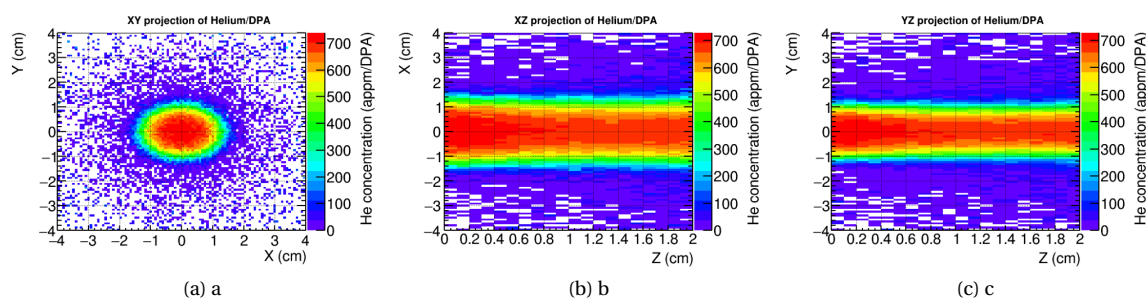


Figure 4.9: The helium production over the lifetime of the Ralentsisseur in the a: XY b: XZ and c: YZ plane.

Figure 4.9a, 4.9b and 4.9c show the distribution of helium, normalized with radiation damage, in the xy-, xz- and yz-plane. Throughout the plate thickness, the peak He concentration in appm/DPA occurs in the center. The He production is a lot wider than the beam, indicating the scattering result. The peak is comparable to the peak He appm/DPA found in other literature. For the European Spallation Source ([40] discussed in section 2.3.4) peak values of 179 He appm/DPA were calculated.

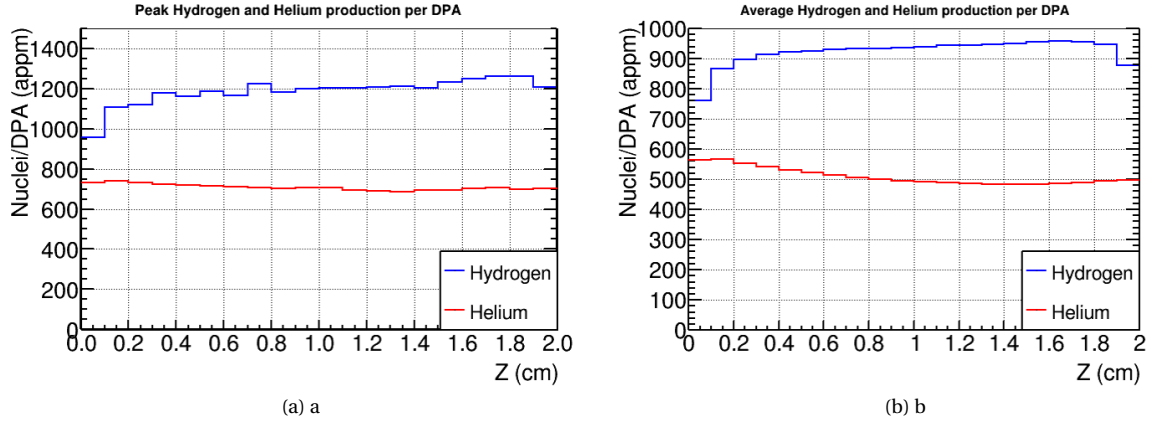


Figure 4.10: The peak (a) and average (b) H and He production/DPA throughout the 2 cm thick tungsten plate. The beam enters the plate at 0.

The peak H appm/DPA amounts to 1270 around  $Z=1.8$  cm and for He the peak appm/DPA is 750 around  $Z=0.2$  cm. These values are high compared to what was achieved in the simulations for the SHiP target in section 2.3.1 where the gas production values amounted to 690 appm/DPA and 305 appm/DPA for hydrogen and helium respectively as well as compared to the European Spallation Source in section 2.3.4, where the results were 850 and 180 appm/DPA for H and He respectively. But the actual DPA and gas production values are quite low compared to those in the SHiP target in section 2.3.1. The maximum helium per DPA ratio in the CSNS target is also a lot lower, 56 and 64 appm/DPA for a uniform and gaussian proton beam. Both in the CSNS and the ESS target DPA and gas production values are much higher, the difference in the gas production per DPA ratio compared to the results for this work could indicate that gas concentrations start saturating before DPA concentration does.

#### 4.2.2. Tungsten and Inermet 180

Due to irradiation, alloying components will be disturbed and transmutation will affect the alloy composition. [58] To investigate the effect of the alloying elements on the radiation damage on tungsten, the same simulations were performed where the plate was IT180 instead of tungsten. Impurities in the lattice can act as trapping sites, which can promote recombination of displacements in the bulk but on the other hand it can also be a point where nucleation of larger defects occurs. Table 4.1 shows the helium, hydrogen and DPA production as discussed for tungsten and for comparison the results for IT180. IT180 has Cu and Ni alloying elements. For example, the effect of these alloying elements on the diffusion of He, H, an interstitial and a vacancy inside tungsten can give more insight on the effects on the production and interaction of DPAs and gas with sinks and the bulk material. Van der Kolk et al. already showed experimentally that Cu is capable of trapping He atoms. Kong et al. performed first-principles calculations to investigate the interaction of transition metals with hydrogen and point defects in tungsten. Cu and Ni attract H because in the presence of the solute atom the change in the charge density results in a site preference. The Cu and Ni vacancy interaction is strongly repulsive. [59, 60] Table 4.1 gives an overview of the peak DPA and gas production values as well as the peak ratios. The DPA production in Inermet 180 is lower which can be attributed to a lower density. The interaction between the alloying elements and the DPAs and gas atoms is not evaluated in FLUKA. To study the influence of alloying elements is therefore necessary to resort to other simulation techniques. First principles simulations can model the interaction between elements and point defects or gas atoms and provide further insight into the evolution of point defects and gas atoms.

In figure 4.11a, the peak DPA values for both materials are given throughout the plate. Tungsten consistently has higher values. This can be attributed to the higher density ( $19.3\text{gcm}^{-3}$  and for IT180  $18\text{gcm}^{-3}$ ). Figure 4.11b shows the H and He production in both materials are more or less the same values from which we can conclude that the difference of  $1.3\text{gcm}^{-3}$  in density is negligible for H and He production. An important sidenote is that Inermet is an alloy and in FLUKA the alloying elements are not taken into account. The density of the material is the main input, which in this case does not reflect the total change in the material-beam interaction. The Cu and Ni elements can affect gas production but also other transmutation elements are more likely to occur than would normally occur in tungsten. For computation of further microstructure



	Tungsten	IT180
Peak DPA	0.0035	0.0033
Peak H (appm)	3.5	3.5
Peak He (appm)	2.5	2.5
Peak H/DPA (appm)	1270	1350
Peak H/DPA (appm)	750	770

Table 4.1: DPA and gas production values for tungsten and IT180 over the lifetime of the Ralentsisseur plate. Simulation by J.Briz Monago.

evolution, Cu and Ni also affect the diffusion coefficient of hydrogen and helium atoms as well as that of vacancies and interstitials.

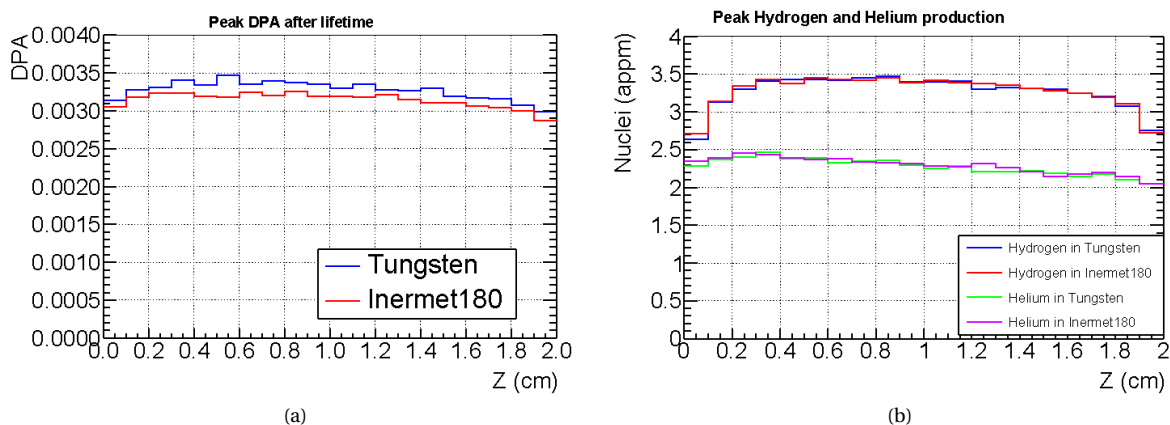


Figure 4.11: The DPA (a) and gas (b) production throughout the 2 cm thick tungsten and IT180 plate. The beam enters the plate at 0.

### 4.3. Effects on Material Properties

The temperatures in the material as well as DPA and gas production remain relatively low compared to similar energy radiation damage cases. Assuming the yield strength with DPA variance that was established by Maloy et al. (figure 2.10b) the yield strength increase due to the DPA production is negligible. Since the maximum DPA does not coincide with the peak H and He production, the most critical combination of DPA and gas production would typically be in between the peak values. Further studies into the interaction between DPA and gas atoms would give more insight into which point would be more critical. Barely any literature discusses DPA and gas production effects in the order of magnitude that is calculated for the Ralentsisseur. 0.07 DPA was achieved by Armstrong et al. and the hardness changed by 0.35 GPa [61, 62]. But irradiation took place at 300 °C which is much higher than the values achieved in the Ralentsisseur during normal operation. Furthermore, Armstrong states that in situ ion irradiation experiments have shown that temperature can have a large effect on the nature of defects that are formed, due to increased mobility of defects and gas atoms. It is also stated that hardness increase saturates below 0.4 DPA which is already a very low damage value but still more than three orders of magnitude more than what is achieved in the Ralentsisseur. Experimental data from such low damage levels are needed to gain more insight on the evolution of radiation damage effects on hardness at lower temperatures and to be able to evaluate the achieved damage. Moreover FLUKA calculates the DPA and gas production based on a 'perfect' lattice with sinks, defects and grainboundaries not taken into account. Also solute atoms that can have a substantial influence on the evolution of radiation damage are not included. Further simulation with other tools such as molecular dynamics could give more accurate DPA and gas production results. From these results the influence of 2D and 3D defects on radiation damage can be evaluated. Korchuganov et al. suggests that molecular dynamics simulation of cascades and their interaction with defects proves they significantly impact cascade evolution [63]. 'LHuillier [64] showed that helium implanted above threshold energy for vacancy formation was fully retained for damage levels above 0.1 DPA where helium implanted below the threshold energy was fully released at 1600°C. This indicates that

helium is bound by vacancies. This is also supported by the work of Lee et al. [65] where DFT simulations show that helium will rather migrate to vacancies than to interstitial or substitutional sites. But since those temperatures are not reached in the Ralentsisseur, He will not be released. Experimental data is required to more accurately evaluate the true effects of the H, He and DPA quantities achieved in this work. He interacts strongly with vacancies but assuming that H embrittlement is the most important effect at these temperatures (see figure 4.2) the most critical effects can occur in a point between the maximum DPA and maximum H production.



## Conclusion and Recommendations

The problem in section 3.1.2 is defined as the interaction of a 2 cm thick tungsten plate with a proton beam inside the Proton Synchrotron. The plate is protecting secondary emission monitor grids from a second high energy proton interaction. Because the new proton beam energy levels are increased from 1.4 to 2 GeV, energy deposition and thermo-mechanical stresses require a new evaluation. The high energy application also calls for investigation of the radiation damage and gas production. This investigation can also result in more accurate estimations of performance, reliability and lifetime of beam intercepting devices besides the Ralentisseur. The FLUKA Monte Carlo simulations are performed where the code does not take into account, existing defects or radiation damage over time. Simulating the distribution of the DPA and gas production over time and coupling diffusion models, the influence of further gas and DPA production on the mobility of DPA and gas can be investigated. The temperatures inside the Ralentisseur plate remain below critical and no cooling is needed. The thermal deformation do not induce plasticity, the Inermet 180 plate is estimated to remain intact. The stress cycles in the highly brittle pure tungsten plate are compared to working conditions of the ESS tungsten target. From test results on the ESS target the usage of tungsten is advised against. As the available experimental data is for much higher DPA and gas production levels than achieved inside the Ralentisseur, a lifetime estimation cannot be extrapolated. However, the DPA and gas production levels do not raise immediate concerns regarding macroscopic property changes and the performance of the Ralentisseur. The beam stopping function is estimated to remain intact. Since temperatures remain relatively low, no annealing will occur. Further research is needed to understand the impact of the remaining gas and DPA on the microstructure and macroscopic properties. The DPA, He and H production are given by simulations for beam impact of 2 GeV protons with Inermet 180 and tungsten. The calculated results cannot be used to make a comparison with tungsten because in the FLUKA Monte Carlo Code, existing defects such as alloying elements are not taken into account. Molecular Dynamics simulations could provide further insight in the error resulting the assumption of a perfect lattice in the material that is initially simulated in FLUKA.

### 5.1. Answering the Research Question

To answer the research question posed in section 1.3 namely: How can radiation damage in materials be incorporated into the design of beam intercepting devices?, subquestions were formed. Based on the findings in this work the answers are composed below.

#### 5.1.1. Radiation Damage Problems in BID's

The reported challenges in BID's are both related to a sudden localized energy deposition and microstructural changes in parts where effects of DPA and gas production occurs. Even values below 1 DPA can have considerable effect on material properties. An example is the 0.25 GPa change in hardness to for 0.07 DPA that was discussed in section 4.3. The hardness of unimplanted tungsten is 7.62 GPa. Hardness rises significantly at 0.4 DPA to 8.45 GPa. Besides the displacement per atom resulting in vacancies and interstitials, gas production can pose a serious problem. Transmutation processes result in hydrogen and helium gas that can both interact with and form defects. If high enough concentrations of gas are found near the surface, blistering can even occur. Besides gas, other transmutation elements for example common in tungsten can be Rhenium, Tantalum and Osmium. These transmutation elements also interact with point defects and gas atoms and

can considerably influence diffusion rates. Alloying elements can have attractive or repulsive interactions with point defects and gas and can hence worsen effects of gas production. Effects of irradiation that are a hot topic in literature are swelling, helium embrittlement, hydrogen embrittlement, irradiation hardening, irradiation creep, bubble formation, blistering and formation of voids.

### 5.1.2. Case Studies in Literature

Many works in literature study radiation damage specifically in fusion reactors. Research projects surrounding the design and commissioning of the ITER and DEMO fusion reactors have made important contributions in generating knowledge in the topic of radiation damage in tungsten. Especially theoretical and computational studies are done, experimental data is less common. For the design of targets for Neutron Spallation Sources relations for mechanical properties with displacement per atom were established. To predict DPA and gas production Monte Carlo Transport simulations were performed for both the China Spallation Neutron Source as well as the European Spallation Source. Beam intercepting devices in high energy applications at CERN have more recently also driven radiation damage research. The Antiproton Decelerator target is an example of radiation damage driven failure in high energy applications. The effects of radiation damage on device lifetime and performance are evaluated after failure. For the design of the SHiP target, thermo-mechanical design studies are done as well as DPA and gas production calculations. It is indicated that further research is required to understand the impact of the DPA and gas values. For the energy production demonstrator target design several metals were tested over an energy range of 0.5 to 120 GeV. The project also includes a materials testing station that aims to maximize DPA and gas production to study radiation damage effects.

### 5.1.3. Investigation Techniques: The State of the Art

When generating experimental data for studying the effects of radiation damage on material properties, radioactivity is a serious health risk to be considered for sample preparation. To decrease radiation risks, samples are made as small as possible so that little irradiation is needed to achieve damage, less activated material is made and lower doses of radiation are emitted to the surroundings. Nano indentation is a common way to determine the hardness. Maloy et al. measure stress-strain curves with compression tests and thermal spectral can give the gas emission for different temperatures and thereby allows to determine the amount of gas that is released with a certain amount of energy and thereby associated with different locations in the lattice (i.e. close to an interstitial or in a vacancy). Simulation methods range over many time and length scales. For example, Density Functional Theory can be used to evaluate electron structures and compute the formation energies of a vacancy near a solute atom in tungsten. These results can then be used for larger scale studies like molecular dynamics simulations to further study their interaction with defects. Monte Carlo simulation can give the evolution of a larger lattice volume with defects by using sampling and the statistical chance that a certain reaction takes place. These methods are just a selection of a broad range of approaches but the simulations range from subatomic and picosecond scale to the a length and timescale of meters and years.

### 5.1.4. Evaluating Radiation Damage Effects on BID Performance and Lifetime at CERN

The engineering department at CERN has a well developed method to achieve thermo-mechanical BID designs. Most common is the usage of ANSYS and sometimes also LS DYNA for changing boundary conditions, large deformations and nonlinear behavior. When radiation damage is expected to have a critical impact on the device lifetime and performance, DPA and gas production are more closely investigated. For example, for the SHiP design in section 2.3.1 the gas production and DPA are computed using FLUKA Monte Carlo code. The peak hydrogen level is compared to experimentally achieved critical values for fusion reactor components. Estimations for microstructural changes due to DPA production are given. To further understand the impact of these values and the simultaneous effects of gas, transmutation elements and DPA, the distributions could be evaluated. Critical damage does not necessarily occur at a maximum DPA or gas concentration. Failure could occur where these values are lower, but their interaction results in critical microstructural changes. Simulations of the formation and behavior of 2D and 3D defects could give an idea of the critical quantities of simultaneous effects of the different radiation damage products. The change of material properties of these effects can then locally be taken into account in finite element thermo mechanical simulations for example, by changing the physical and mechanical properties in the material model.

## 5.2. Recommendations

To improve the studies on Inermet 180, further characterization is needed. This would be very significant for further radiation damage studies on the Ralentsisseur. Further benchmarking of low radiation damaged materials would make it possible to relate the calculation results to a change in material properties. If the FLUKA simulations are used to also calculate the formation of further transmutation elements (TE's), the interaction between these elements and the gas atoms could be studied. For example, Zhao et al. [22] simulated the TE interactions with He and H in a pure tungsten lattice. The attraction between TEs and H at the SS site is stronger than at OIS sites, the attraction at TIS sites being the weakest. The attractive interaction between Os and He is stronger than that of Re and He, where Ta and He have a repulsive interaction. FLUKA simulations calculating the production of TE's like Re, Os and Ta can allow for integration of these simulation results into the evaluation of tungsten and gain more insight on their effects on the microstructure evolution. Precipitates rich in Cu and P, microvoids and metal carbides are responsible for hardening. Inermet 180 has Cu as an alloying element more research is required to understand the impact of this effect. [50] More insight could be gained from plotting the DPA and gas production over time. For these simulations the total beam interaction over the Ralentsisseur lifetime is plotted. With the overview of the DPA and gas production for example per year, structural changes in the material and their effect on the generation and evolution of further radiation damage and gas could be investigated. Furthermore, since FLUKA assumes a perfect crystal, investigating the defect and gas distribution over time could give more insight in the effects of radiation damage on cascade evolution and the errors resulting from neglecting prior damage in the material.



# Bibliography

- [1] G Federici, W Biel, MR Gilbert, R Kemp, N Taylor, and R Wenninger. European demo design strategy and consequences for materials. *Nuclear Fusion*, 57(9):092002, 2017.
- [2] AV Nikitin, GD Tolstolutszkaya, VV Ruzhytskyi, VN Voyevodin, IE Kopanets, SA Karpov, RL Vasilenko, and FA Garner. Blister formation on 13cr2monbv ferritic-martensitic steel exposed to hydrogen plasma. *Journal of Nuclear Materials*, 478:26–31, 2016.
- [3] Thomas M Orlando, Brant Jones, Carol Paty, Micah J Schaible, John R Reynolds, Phillip N First, Stephen K Robinson, Valeria La Saponara, and Esther Beltran. Catalyst: Radiation effects on volatiles and exploration of asteroids and the lunar surface. *Chem*, 4(1):8–12, 2018.
- [4] Massimo Florio, Stefano Forte, and Emanuela Sirtori. Forecasting the socio-economic impact of the large hadron collider: A cost–benefit analysis to 2025 and beyond. *Technological Forecasting and Social Change*, 112, 2016.
- [5] Report on the impacts of large research infrastructures on economic innovation and on society: Case studies at cern. Technical report, Paris, 2014. URL <https://cds.cern.ch/record/1708387>.
- [6] K Parodi, A Ferrari, F Sommerer, and H Paganetti. Clinical ct-based calculations of dose and positron emitter distributions in proton therapy using the fluka monte carlo code. *Physics in Medicine and Biology*, 52(12):3369, 2007.
- [7] Christiane Lefèvre. The cern accelerator complex. complexe des accélérateurs du cern. Dec 2008. URL <https://cds.cern.ch/record/1260465>.
- [8] Atlas Collaboration et al. Observation of a new particle in the search for the standard model higgs boson with the atlas detector at the lhc. *arXiv preprint arXiv:1207.7214*, 2012.
- [9] Technical report.
- [10] G. Romagnoli F Nuiry. Ps ring ralentisseur functional specification. (edms 1746673). Report, CERN, 2017.
- [11] G. Romagnoli F Nuiry. Space reservation request new ps ring ralentisseur. (edms 1746714). Report, CERN, 2017.
- [12] Jaakko Johannes Esala. *Preliminary design of the new Proton Synchrotron Internal Dump core*. PhD thesis, Aalto U., 2017.
- [13] H. Damerou. Lhc injectors upgrade, technical design report, vol. i: Protons. (cern-acc-2014-0337). Electronic article, CERN, 2014. URL <http://cds.cern.ch/record/1976692>.
- [14] W Herr. Proceedings of the cas-cern accelerator school: Advanced accelerator physics course, trondheim, norway, 18-29 aug 2013. *arXiv preprint arXiv:1601.07311*, 2016.
- [15] Michel Arruat and Michel Martini. The new standard method to measure emittances in the ps transfer lines. Technical report, CM-P00059366, 1992.
- [16] Technical report.
- [17] Alessandro Bertarelli. Beam-induced damage mechanisms and their calculation. *arXiv preprint arXiv:1608.03056*, 2016.
- [18] Christopher Race. *The modelling of radiation damage in metals using Ehrenfest dynamics*. Springer Science & Business Media, 2011.

- [19] Gary S. Was. *Fundamentals of radiation materials science : metals and alloys*. Springer, Berlin ; New York, 2007. ISBN 9783540494713 (hbk.) 3540494715 (hbk.). URL [Tableofcontentshttp://www.loc.gov/catdir/toc/fy0802/2007922926.html](http://www.loc.gov/catdir/toc/fy0802/2007922926.html)[Publisherdescriptionhttp://www.loc.gov/catdir/enhancements/fy0824/2007922926-d.html](http://www.loc.gov/catdir/enhancements/fy0824/2007922926-d.html).
- [20] U Fano. Penetration of protons, alpha particles, and mesons. *Annual Review of Nuclear Science*, 13(1): 1–66, 1963.
- [21] A Yu Konobeyev, U Fischer, Yu A Korovin, and SP Simakov. Evaluation of effective threshold displacement energies and other data required for the calculation of advanced atomic displacement cross-sections. *Nuclear Energy and Technology*, 3(3):169–175, 2017.
- [22] Qiang Zhao, Zheng Zhang, Yang Li, and Xiao-Ping Ouyang. Effects of transmutation elements in tungsten as plasma-facing material. *arXiv preprint arXiv:1706.03252*, 2017.
- [23] Roger Eckhardt. Stan ulam, john von neumann, and the monte carlo method. *Los Alamos Science*, 15 (131-136):30, 1987.
- [24] T Sato et al. Phits particle and heavy ion transport code system, 2017.
- [25] Jan M Zazula. From particle cascade simulations (fluka) to finite element heat transfer and structural deformation analyses (ansys). Technical report, 1995.
- [26] NV Mokhov and F Cerutti. Beam-material interaction. *arXiv preprint arXiv:1608.02476*, 2016.
- [27] Wayne D Newhauser and Rui Zhang. The physics of proton therapy. *Physics in Medicine & Biology*, 60 (8):R155, 2015.
- [28] M Fukumoto, Y Ohtsuka, Y Ueda, M Taniguchi, M Kashiwagi, T Inoue, and K Sakamoto. Blister formation on tungsten damaged by high energy particle irradiation. *Journal of Nuclear Materials*, 375(2):224–228, 2008.
- [29] Marco Calviani, Alexandre Pascal Perez, Heinz Vincke, Robin Betemps, Valentina Venturi, A Pacholek, Jean-Louis Grenard, Aniko Judit Rakai, Roberto Rinaldesi, Claudia Christina Strabel, et al. Conceptual design of the ship target and target complex. Technical report, 2015.
- [30] C Torregrosa, A Perillo-Marcone, and M Calviani. Designs characteristics and main inherent concerns of the antiproton decelerator target. Technical report, 2015.
- [31] Moritz Guthoff, Konstantin Afanaciev, Anne Dabrowski, Wim de Boer, Wolfgang Lange, Wolfgang Lohmann, and David Stickland. Radiation damage in the diamond based beam condition monitors of the cms experiment at the large hadron collider (lhc) at cern. *Nuclear Instruments and Methods in Physics Research Section A: Accelerators, Spectrometers, Detectors and Associated Equipment*, 730:168–173, 2013.
- [32] Marc Tavlet, Anne Fontaine, and Helmut Schonbacher. *Compilation of radiation damage test data, pt.2. Index des resultats d'essais de radioresistance, t.2; 2nd ed.* CERN Yellow Reports: Monographs. CERN, Geneva, 1998. URL <https://cds.cern.ch/record/357576>.
- [33] Michael Moll, RD50 Collaboration, et al. Development of radiation hard sensors for very high luminosity colliders-cern-rd50 project. *Nuclear Instruments and Methods in Physics Research Section A: Accelerators, Spectrometers, Detectors and Associated Equipment*, 511(1-2):97–105, 2003.
- [34] K Wick, D Paul, P Schroder, V Stieber, and B Bicken. Recovery and dose rate dependence of radiation damage in scintillators, wavelength shifters and light guides. *Nuclear Instruments and Methods in Physics Research Section B: Beam Interactions with Materials and Atoms*, 61(4):472–486, 1991.
- [35] CMS collaboration et al. Technical proposal for the upgrade of the cms detector through 2020. Technical report, 2011.
- [36] Vitaly S Pronskikh, Nikolai V Mokhov, Igor Novitski, and Sergey I Tyutyunnikov. Energy production demonstrator and material testing station optimization for megawatt proton beams. *Annals of Nuclear Energy*, 109:692–697, 2017.

- [37] W Yin, QZ Yu, YL Lu, SL Wang, JF Tong, and TJ Liang. The expected radiation damage of csns target. *Journal of Nuclear Materials*, 431(1-3):39–43, 2012.
- [38] SA Maloy, MR James, W Sommer Jr, GJ Willcutt Jr, M Lopez, TJ Romero, and Mychailo B Toloczko. The effect of 800 mev proton irradiation on the mechanical properties of tungsten at room temperature and at 475° c. *Journal of Nuclear Materials*, 343(1-3):219–226, 2005.
- [39] Dong-Dong Pan, Tai-Ran Liang, Wen Yin, and Ze-En Yao. Calculation of hydrogen and helium concentrations for csns target. *Chinese Physics C*, 40(3):037004, 2016.
- [40] Tomas Mora, Fernando Sordo, Adrian Aguilar, Luis Mena, Maite Mancisidor, Jorge Aguilar, Gorka Bakedano, Inigo Herranz, Paula Luna, Miguel Magan, et al. An evaluation of activation and radiation damage effects for the european spallation source target. *Journal of Nuclear Science and Technology*, 55(5):548–558, 2018.
- [41] D. Cotte R. Steerenberg. Ps beam spot sizes for the design of new internal beam dumps. (edms 1612293). Report, CERN, 2017.
- [42] A Bertarelli, N Mariani, L Peroni, A Dallochio, V Boccone, F Cerutti, F Carra, and Martina Scapin. Limits for beam induced damage: reckless or too cautious? Technical report, 2011.
- [43] Plansee. Home, Nov 2017. URL <https://www.plansee.com/en/materials/tungsten-heavy-metal.html>.
- [44] J.A. Briz V. Vlachoudis. Fluka studies for the ps ralentisseur. (edms 1887747). Report, CERN, 2017.
- [45] Alexandre Ouzia, Adam Balogh, Cesare Maglioni, and Ivo Leitao. *Feasibility study of a vertical slit for the LBS line of the Linac4*. PhD thesis, Sep 2012. URL <https://cds.cern.ch/record/1516985>. Presented 31 Aug 2012.
- [46] R. Welschen F. Nuiry. Ansys simulations quality plan for the sti-tcd section. (edms 1936874). Report, CERN, 2018.
- [47] J. Esala. Thermomechanical evaluation of the current ps ralentisseur. (edms 1753282). Report, CERN, 2017.
- [48] OV Ogorodnikova, Yu Gasparyan, V Efimov, J Grzonka, et al. Annealing of radiation-induced damage in tungsten under and after irradiation with 20 mev self-ions. *Journal of Nuclear Materials*, 451(1-3):379–386, 2014.
- [49] Jemila Habainy, Srinivasan Iyengar, Y Lee, and Y Dai. Fatigue behavior of rolled and forged tungsten at 25°, 280° and 480° c. *Journal of Nuclear Materials*, 465:438–447, 2015.
- [50] H Ullmaier. Radiation damage in metallic materials. *Mrs Bulletin*, 22(4):14–21, 1997.
- [51] Giuseppe Battistoni, F Cerutti, A Fasso, A Ferrari, S Muraro, J Ranft, S Roesler, and PR Sala. The fluka code: Description and benchmarking. In *AIP Conference proceedings*, volume 896, pages 31–49. AIP, 2007.
- [52] P Schoofs, F Cerutti, A Ferrari, and G Smirnov. Benchmark of the fluka model of crystal channeling against the ua9-h8 experiment. *Nuclear Instruments and Methods in Physics Research Section B: Beam Interactions with Materials and Atoms*, 355:374–377, 2015.
- [53] Till Tobias Bohlen, F Cerutti, M Dosanjh, A Ferrari, Irena Gudowska, A Mairani, and JM Quesada. Benchmarking nuclear models of fluka and geant4 for carbon ion therapy. *Physics in Medicine & Biology*, 55(19):5833, 2010.
- [54] F. Cerutti V. Vlachoudis, J.A. Briz. Modelization of radiation-induced damage in fluka and material damage estimates for cern injectors and future facilities. Report, CERN, 2017.
- [55] OV Ogorodnikova, B Tyburska, V Kh Alimov, and K Ertl. The influence of radiation damage on the plasma-induced deuterium retention in self-implanted tungsten. *Journal of Nuclear Materials*, 415(1):S661–S666, 2011.

- [56] RE Stoller. Primary damage formation in irradiated materials. *JOM*, 48(12):23–27, 1996.
- [57] Jens Lindhard, Morten Scharff, and Hans E Schiøtt. *Range concepts and heavy ion ranges*. Munksgaard Copenhagen, 1963.
- [58] LK Mansur. Theory and experimental background on dimensional changes in irradiated alloys. *Journal of Nuclear Materials*, 216:97–123, 1994.
- [59] Xiang-Shan Kong, Xuebang Wu, Yu-Wei You, CS Liu, QF Fang, Jun-Ling Chen, G-N Luo, and Zhiguang Wang. First-principles calculations of transition metal–solute interactions with point defects in tungsten. *Acta Materialia*, 66:172–183, 2014.
- [60] Xiang-Shan Kong, Xuebang Wu, CS Liu, QF Fang, QM Hu, Jun-Ling Chen, and G-N Luo. First-principles calculations of transition metal solute interactions with hydrogen in tungsten. *Nuclear Fusion*, 56(2):026004, 2015.
- [61] DEJ Armstrong, X Yi, EA Marquis, and SG Roberts. Hardening of self ion implanted tungsten and tungsten 5-wt% rhenium. *Journal of Nuclear Materials*, 432(1-3):428–436, 2013.
- [62] DEJ Armstrong, AJ Wilkinson, and SG Roberts. Mechanical properties of ion-implanted tungsten–5 wt% tantalum. *Physica Scripta*, 2011(T145):014076, 2011.
- [63] AV Korchuganov, VM Chernov, KP Zolnikov, DS Kryzhevich, and Sergey Grigorievich Psakhie. Md simulation of primary radiation damage in metals with internal structure. *Inorganic Materials: Applied Research*, 7(5):648–657, 2016.
- [64] Pierre-Emile Lhuillier, Taieb Belhabib, Pierre Desgardin, Blandine Courtois, Thierry Sauvage, Marie-France Barthe, Anne-Lise Thomann, Pascal Brault, and Yves Tessier. Trapping and release of helium in tungsten. *Journal of Nuclear Materials*, 416(1-2):13–17, 2011.
- [65] Seung-Cheol Lee, Jung-Hae Choi, and June Gunn Lee. Energetics of he and h atoms with vacancies in tungsten: First-principles approach. *Journal of Nuclear Materials*, 383(3):244–246, 2009.
- [66] Marija Cauchi, RW Assmann, A Bertarelli, Federico Carra, F Cerutti, L Lari, S Redaelli, P Mollicone, and N Sammut. mechanical response of large hadron collider collimators to proton and ion beam impacts. *Physical Review Special Topics-Accelerators and Beams*, 18(4):041002, 2015.



# List of Figures

1.1	Optical micrographs of blisters on the surface of 95% deformed 13Cr2MoNbVB steel after irradiation with hydrogen plasma to $2 \cdot 10^{24} H/m^2$ at 275 (left), 305 (center) and 323 K (right). The micrographs are made for studying sputtering-induced erosion of plasma-facing materials (PFMs) for future commercial reactors. The scale is the same for all micrographs. [2] . . . . .	1
1.2	Monte Carlo calculated dose deposition (left) against the planned treatment (right). The top row shows a posterior-anterior field delivering 2 GyE to a tumor. The rainbow colour-bar displays dose values in mGy. The black-white colour-bar represents the HU map arbitrary rescaled for display purposes. [6] . . . . .	2
1.3	The CERN accelerator and experiment complex (modified from [7]) . . . . .	3
1.4	a: Proton Synchrotron (r=72m) scheme showing the SEM-grid and Ralentsisseur positions. b: Working mechanism of the Ralentsisseur indicated with previous technical drawings [12]. . . . .	4
2.1	The history of each neutron is generated by making various decisions about the physical events that occurs as the neutron goes along. [23] . . . . .	10
2.2	Overview of the most important energy deposition mechanisms for thermo-mechanical studies using FLUKA energy deposition maps as a thermal load. . . . .	11
2.3	SEM photograph of the tungsten samples with (a) 0 DPA, (b) 0.3 DPA, and (c) 3.5 DPA damage after mixed H+, C+ ion beam irradiation. [28] . . . . .	12
2.4	The figure shows the assumed beam sweep footprint at the longitudinal position corresponding to the SHiP target. [29] . . . . .	13
2.5	The figure shows the energy density along the Z direction but averaged along the horizontal direction 2 cm around the beam centre. [29] . . . . .	14
2.6	The figure shows the maximum DPA along the longitudinal (Z) direction. [29] . . . . .	14
2.7	Overview of the most important energy deposition mechanisms for thermo-mechanical studies using FLUKA energy deposition maps as a thermal load. [29] . . . . .	14
2.8	a: Helium ( ${}^2_2\text{He}_4$ and ${}^2_2\text{He}_3$ ) production in the targets. b: Displacement per atom (DPA) volume in the targets. . . . .	16
2.9	DPA (top), H (left) and He (right) production in the ESS target after 5 years of operation, Proton beam profiles along horizontal and vertical directions employed for the calculations. Such profiles correspond to those contained within the current machine specification. [40] . . . . .	17
2.10	a: Calculated helium and hydrogen content of the samples plotted as a function of dose. b: Graph plotting 0.2% yield stress vs. dose for compression tests on tungsten irradiated up to 23 DPA at 50–270°C and a test temperature of 25°C.[38] . . . . .	18
2.11	a: Graph showing engineering stress/strain curves for tungsten irradiated to 4.6 DPA and compression tested at room temperature. Tests are divided into specimens with 3.2 mm diameter and 2.6 mm diameter. The two different size specimens were made from different heats of tungsten. Data were gathered continuously. The plot markers are an aid to distinguishing between the different tests. b: Graph showing engineering stress/strain curves for tungsten tested in compression at room temperature after irradiation in a proton beam from doses ranging from 0 DPA to 23 DPA. Data were gathered continuously. The plot markers are an aid to distinguishing between the different tests.[38] . . . . .	18
3.1	A stresswaves in the Ralentsisseur tungsten plate from intercepting a 2 GeV proton beam. . . . .	22
3.2	a: FLUKA energy deposition map for coarse binning. High Luminosity LHC beam and IT180.[44] b: FLUKA energy deposition map for fine binning. High Luminosity LHC beam and IT180. [44] .	23
3.3	a: Worst case scenario fluence of the particles going into the Ralentsisseur plate and coming out of the plate. [44] b: Energy spectra of proton beam particles incident and exciting the Ralentsisseur in comparison with machine acceptance.[44] . . . . .	24

3.4	Overview of the Ralentsisseur ANSYS project including all different modules for thermal, structural, steady state and energycheck simulations. . . . .	25
3.5	Example of FLUKA data file for ANSYS energy deposition input. [44] . . . . .	26
3.6	The fixed nodes in the simulation are a line of nodes in the center on the side and one single node on the top. . . . .	26
3.7	a: Top half of plate sectioned with radiation and conduction boundary conditions applied. b: Plate mesh of half the plate. A symmetry is assumed over the center xz-plane and the mesh remains constant throughout the thickness of the body. . . . .	26
3.8	Mesh convergence studies results. The maximum temperature varying over mesh size. . . . .	27
3.9	a: Maximum temperature from a single HLLHC pulse beam interaction. b: Steady state temperature from a single HLLHC pulse beam interaction. . . . .	29
3.10	Inermet 180 thermal transient simulation of a single HLLHC beam pulse interaction. . . . .	29
3.11	Thermal transient simulation of continuous beam pulse interactions until steady state is reached. . . . .	30
3.12	a: Directional and equivalent Von Mises stresses in the node with the most critical stresses from a single HLLHC pulse beam interaction. b: Tensile stresses and Von Mises Stress in Inermet 180 from a single HLLHC pulse beam interaction. . . . .	30
3.13	a: Minimum and Maximum Principal stresses in pure tungsten from a single HLLHC pulse beam interaction. b: Tensile stresses in pure tungsten from a single HLLHC pulse beam interaction. . . . .	30
3.14	The Von Mises Stresses for the HLLHC beam interaction with Inermet 180 at $\sigma_{max}$ . . . . .	31
3.15	Wohler diagram for rolled and forged tungsten at 25 °C. [49] . . . . .	31
4.1	HLLHC-beam proton distribution used to calculate DPA, H and He production. . . . .	33
4.2	Approximate range of temperatures (normalized to the melting point $J_m$ ) where the radiation-damage effects described in the section on Changes of Macroscopic Properties occur. Irradiation growth is restricted to noncubic metals. Hydrogen embrittlement is expected only for cases with extremely high production rates for hydrogen isotopes such as in spallation target materials. [50] . . . . .	34
4.3	A proton travelling through liquid Argon and created particle showers and cascades from interaction.[54] . . . . .	36
4.4	The average (a) and peak (b) DPA throughout the 2 cm thick tungsten plate. The beam enters the plate at 0. . . . .	37
4.5	The DPA production over the lifetime of the Ralentsisseur in the a: XY b: XZ and c: YZ plane. . . . .	37
4.6	The dose (in Grey per pulse) on equipment surrounding the Ralentsisseur. (courtesy of J. Briz Monago) . . . . .	38
4.7	The average (a) and peak (b) hydrogen and helium gas throughout the 2 cm thick tungsten plate. The beam enters the plate at 0. . . . .	38
4.8	The hydrogen production over the lifetime of the Ralentsisseur in the a: XY b: XZ and c: YZ plane. . . . .	39
4.9	The helium production over the lifetime of the Ralentsisseur in the a: XY b: XZ and c: YZ plane. . . . .	39
4.10	The peak (a) and average (b) H and He production/DPA throughout the 2 cm thick tungsten plate. The beam enters the plate at 0. . . . .	40
4.11	The DPA (a) and gas (b) production throughout the 2 cm thick tungsten and IT180 plate. The beam enters the plate at 0. . . . .	41

# List of Tables

2.1	DPA and gas production values for a 1.6 GeV 100 kW gaussian and uniformly shaped proton beam operating 5000 hours per year. . . . .	16
3.1	Summary of material properties of pure tungsten and IT180 (properties obtained from, Plansee SE, CES Selector 2015 and MPDB v7.71)[43]. More extensive list of material properties and sources can be found in appendix A.1. . . . .	22
3.2	PS beam properties for the design of new internal beam dumps.[41] . . . . .	23
3.3	Relative errors between FLUKA and ANSYS energy and power deposition for both tungsten and IT180. . . . .	27
3.4	An overview of the results for the thermal, structural and steady state simulations for all beams and including the analytically derived adiabatic predictions. . . . .	28
4.1	DPA and gas production values for tungsten and IT180 over the lifetime of the Ralentisseur plate. Simulation by J.Briz Monago. . . . .	41
1	. . . . .	57
2	<sub>1</sub> 1.5mm sheet recrystallized at 1399°C, WORSTCASE. <sub>2</sub> Equivalent alloy "WH9570C". <sub>3</sub> Ho et al. <sub>4</sub> Binkele Note: For future work, it may be necessary to further evaluate the variance of Inermet properties over a temperature range. E.g. Cauchi [66] has done measurements from 0 to 1450°C. Since the emmissivity for Inermet 180 was not available, the emmissivity constant for pure tungsten was used . . . . .	57



# **Appendices**



## A.1 Extensive list of material properties and sources

Property	Pure Tungsten			
	MPDB v7.71		Plansee producer	
	20°C	800°C	20°C	800°C
Density (kgm <sup>-3</sup> )	19290	19090	19300	-
Young's Modulus (GPa)	400	364	405	370
Poisson's Ratio	0.282	0.292	0.28	-
Thermal Conductivity (Wm <sup>-2</sup> ·K <sup>-1</sup> )	174 <sub>3</sub> , 175 <sub>4</sub>	116 <sub>3</sub> , 97 <sub>4</sub>	164	120
Emmissivity	0.059 <sub>2</sub>	-	0.02	0.13
Specific Heat (Jkg <sup>-1</sup> ·°C <sup>-1</sup> )	132	150	130	-
Mean Coefficient of Thermal Expansion (μ°C <sup>-1</sup> )	4.43	4.8	4.2	4.45
Yield Strength (MPa)	1320	76 <sub>1</sub>	1350	600
Maximum Service Temperature (°C)	-	-	825-1210	

Table 1

Property	IT180			
	MPDB v7.71		Plansee producer	
	20°C	800°C	20°C	600°C
Density (kgm <sup>-3</sup> )	18000	-	18000	-
Young's Modulus (GPa)	355	-	360	-
Poisson's Ratio	0.28	-	-	-
Thermal Conductivity (Wm <sup>-2</sup> ·K <sup>-1</sup> )	135	-	110	-
Emmissivity	-	-	-	-
Specific Heat (Jkg <sup>-1</sup> ·°C <sup>-1</sup> )	135	-	-	-
Mean Coefficient of Thermal Expansion (μ°C <sup>-1</sup> )	4.45	-	5.23	5.45
Yield Strength (MPa)	533	-	615	-
Maximum Service Temperature (°C)	793-1160		-	-

Table 2:

<sub>1</sub> 1.5mm sheet recrystallized at 1399°C, WORSTCASE.

<sub>2</sub> Equivalent alloy "WH9570C".

<sub>3</sub> Ho et al.

<sub>4</sub> Binkele

Note: For future work, it may be necessary to further evaluate the variance of Inermet properties over a temperature range. E.g. Cauchi [66] has done measurements from 0 to 1450°C.

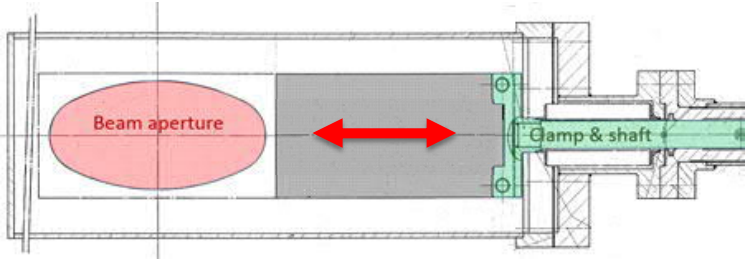
Since the emmissivity for Inermet 180 was not available, the emmissivity constant for pure tungsten was used





## A.2 Beam specifications

Project leader name	François-Xavier Nuiry	Other contact person	Romy Welschen
Time frame	-	Budget code	-
Project Framework / description	Design of dedicated internal dump (Ralentisseur) for the PS.		
-Purpose of the device -Motivations -Details about operation	<ul style="list-style-type: none"> <li>- In case SEM-grids are used for beam studies, the Ralentisseur is needed to dump the beam after one turn.</li> <li>- The current Ralentisseur is obsolete.</li> <li>- A pneumatic system places the dump material in the beamline. The system is interlocked with the placement of the SEM-grids.</li> </ul>		
How many devices? How many spares?	1 device, 0 spares		
Is there an existing device? Identification number?	 <p>Yes</p>		
-Device location(s)? -Available space? -Beam location / ground	<ul style="list-style-type: none"> <li>- SS12</li> <li>- SS12 or SS75</li> </ul>		
Links to documents about existing device. Access rights.	<i>CATIA-Smarteam</i> <i>CDD numbers</i> <i>EDMS Documents 1746673, 1746714, 1753282,</i> <i>MTF /Infor EAM</i> <i>PDF documents</i>		
Any device pictures?	Yes (G:\Departments\EN\Groups\STI\TCD\PS_Complex\PS\PS_Ralentisseur)		
<b>Beam Parameters (for Fluka and thermo-mechanical simulations). Worst supposed scenario</b>			
Beam cycle description Cycle sketch / graph			
Particles to consider	Protons		
Intensity	5, 2.4 and $1.6 \times 10^{13}$ (ACCID, HLLHC and BCMS)		
Beam Energy (GeV)	2		
Bunch time (ns)	575		
Bunch spacing (ns)	-		
Pulse period (s)	30		
Pulse time (ns)	575		
Number of bunch per pulse	1		
How many cycles to take into account in simulations (life cycle)	Continuously until steady state		
Beam size $\sigma_x$ (mm)	8.25, 4.42 and 3.51 (ACCID, HLLHC and BCMS)		
Beam size $\sigma_y$ (mm)	6.09, 3.66 and 3.22 (ACCID, HLLHC and BCMS)		

Beam impact location	SS12 or SS75
Any other info?	
Device Design Requirements	
Materials to consider ?	Inermet 180
Design to consider ?	
Desired movements (sketch)	<p>Horizontal translation of the plate blocking beam aperture</p> 
Strokes (mm)	160
Positioning accuracy (mm)	1
Time to cover the stroke (s) Or Speed (m/s)	1 s
Frequency of the movement	1
Device location precision / beam (mm)	2
Expected device life time (years)?	15 years
Vacuum requirement (mBar)	-
Device environment / working conditions	
Ambient temperature (°C)	22
Ambient dose rate (μSv/h)	How hot is the actual environment? Activation of the BID itself will be studied later
Presence of sensitive equipment around BID	R2E / cryo hazard / equipment close to BID requiring frequent intervention
Known contamination issues	-
Access to BID with vehicles? Handling?	Same as acces to SS 12 or SS 75

